Durham E-Theses

Quantum algorithms for event generation in high-energy collisions

KHADEEJAH BEPARI

How to cite:

BEPARI, KHADEEJAH (2024) Quantum algorithms for event generation in high-energy collisions. Doctoral thesis, Durham University.

Use policy

The full-text may be used and/or reproduced, and given to third parties in any format or medium, without prior permission or charge, for personal research or study, educational, or not-for-profit purposes provided that:

- a full bibliographic reference is made to the original source
- a https://etheses.durham.ac.uk/id/eprint/15643/ is made to the metadata record in Durham E-Theses
- the full-text is not changed in any way

The full-text must not be sold in any format or medium without the formal permission of the copyright holders.

Please consult the full Durham E-Theses policy for further details.

Academic Support Office, The Palatine Centre, Durham University, Stockton Road, Durham, DH1 3LE
e-mail: e-theses.admin@durham.ac.uk Tel: +44 0191 334 6107
https://etheses.durham.ac.uk

Quantum algorithms for event generation in high-energy collisions

Khadeejah Bepari

A Thesis presented for the degree of
Doctor of Philosophy

Institute for Particle Physics Phenomenology
Department of Physics
Durham University
United Kingdom

July 2024

Quantum algorithms for event generation in high-energy collisions

Khadeejah Bepari

Submitted for the degree of Doctor of Philosophy

July 2024

Abstract: The efficient simulation of accurate collider data at modern collider experiments will be crucial for the detection of Beyond the Standard Model signatures in the search for new physics. Simulation of collision processes at hadron colliders like the LHC are carried out by Monte Carlo event generators which simulate the evolution from an initial hard scattering event, downwards in energy scales, towards the formation of long lived particles. However, as we enter a new era of higher luminosity experiments, accurate simulations of these pseudo-event generated data will become further computationally intensive with the vast amounts of data to generate. With the rapid development of quantum computing hardware, quantum computation offers itself as an alternative computing paradigm that may be harnessed to provide a natural framework to model several physical processes in high-energy physics, where the inherent quantum features of the device may be exploited to provide speedups or enhance current simulations. In this thesis, we present general and extendable quantum algorithms for two crucial parts of event generation: the calculation of matrix elements for the hard interaction and the QCD parton shower stage. First, a novel algorithm is proposed for the calculation of helicity amplitudes by outlining a proposal of constructing helicity spinors directly on a quantum circuit and manipulating the spinors to compute helicity amplitudes. This was used to calculate multiple helicity amplitudes for simple tree level scattering processes simultaneously as a proof-of-principle demonstration. The second algorithm outlines a proposal for a Monte Carlo-inspired parton shower algorithm which was used to simulate two shower steps of a simplified QCD model. The final algorithm extends the quantum parton shower algorithm onto a quantum walk framework which demonstrates significant scaling improvements, simulating more realistic shower depths. These algorithms utilise the quantum computers' ability to remain in a quantum state throughout the computation and represents a first step towards a quantum computing algorithm describing full collision events at the LHC.

Contents

List of Figures

Declaration

The work in this thesis is based on research carried out at the Institute for Particle Physics Phenomenology, Department of Physics, Durham University. No part of this thesis has been submitted elsewhere for any other degree or qualification. It is based on my own work, and on work undertaken in collaboration with the other co-authors of the following publications:

- Chapters 4 and 5 contain results which have been published in: **K. Bepari** S. Malik, M. Spannowsky and S. Williams, *Towards a quantum computing algorithm for helicity amplitudes and parton showers, Phys. Rev. D* **103** (2021) 076020, `[2010.00046]`.
- Chapter 6 contains results which have been published in: **K. Bepari**, S. Malik, M. Spannowsky and S. Williams, *Quantum walk approach to simulating parton showers, Phys. Rev. D* **106**(2022)056002, `[2109.13975]`.

Note that the structure of this thesis, as well as content from chapters 5 and 6, was inspired by the recently published thesis of one of the co-authors (S. Williams) from the above papers [5].

Copyright © 2024 Khadeejah Bepari.
The copyright of this thesis rests with the author. No quotation from it should be published without the author's prior written consent and information derived from it should be acknowledged.

Acknowledgements

I would like to start by thanking my supervisor, Michael Spannowsky, for introducing me to the world of quantum computing and the exciting applications of quantum computing to high-energy physics. It was a unique and amazing opportunity to delve into a relatively unexplored field of research, thus making me part of a very small group of people within the Institute for Particle Physics Phenomenology working in this area. This was challenging yet eye-opening and watching the field rapidly grow over the years of undertaking my PhD has been a pleasure. The interdisciplinary nature of the field of research has also allowed me satisfy my curiosity by allowing myself to cross into fields I had never expected to explore before. I am thankful for his guidance and for the opportunities created in this journey, as well patience and understanding for my unexpected circumstances. Finally, I am grateful for the environment created by both the academic staff and my peers, where I could fully enjoy the scintillating discussions at the talks held by them.

“*What we observe is not nature itself, but nature exposed to our method of questioning.*”

— from *Physics and Philosophy: The Revolution in Modern Science* by Werner Heisenberg

Dedicated to

Hamidun Jahan Bepari

Chapter 1

Introduction

The Standard Model (SM) is the most well-tested description of nature that governs the dynamics of fundamental particles on microscopic scales giving accurate predictions on distances smaller than $\mathcal{O}\left(10^{-18}\text{m}\right)$, with its renowned success culminating in the detection of the Higgs bosons in 2012 by the ATLAS [6] and CMS [7] experiments at the LHC. Despite this, the theory is largely believed to be incomplete as several outstanding issues remain such as the matter-antimatter asymmetry observed in the universe, the strong CP problem, the Hierarchy problem along with many other fundamental puzzles of nature not accounted for by the SM. This has initiated an active research field over recent decades seeking extensions to the currently accepted SM, known as Beyond the Standard Model (BSM) models, to successfully address these questions.

Modern collider experiments such as the Large Hadron Collider (LHC) at CERN depend heavily on Monte Carlo event generators to accurately simulate the complicated particle collisions as well detector responses at these colliders. In the coming era of higher energy and higher luminosity colliders, accurate simulations of the background processes of the SM will be crucial to point to any indication of BSM physics. Yet matching the amount of vast data generated from these high luminosity colliders will be computationally challenging. This has motivated the search for alternative computational tools to possibly enhance existing algorithms or propose completely novel algorithms that would be better-suited to the highly-complex, large multiplicity calculations. With the rapid development of quantum computational hardware, quantum computing (QC) provides a prime candidate for this. Although still at an early stage, numerous proposals for applications of QC to high-energy physics (HEP) have already been developed, with applications ranging from simulation of quantum field theories [8–12], and collision events [13, 14], to event classification and analysis [15–19]. However, hardware development remains in its infancy, allowing only Noisy Intermediate-Scale Quantum (NISQ) devices available to use [20], requiring a careful approach to develop resource-efficient quantum algorithms for implementation on near-future devices.

In this thesis, we consider the application of QC to the calculation of two major stages of event generation known as the hard interaction and parton shower process, both time-consuming parts, forming bottlenecks in the generation of data at the LHC. First we introduce the theoretical background necessary to introduce the main body of research outlined in this thesis, this includes both particle physics and QC in chapters 2 and 3 respectively. In chapter 4 we introduce a quantum algorithm to compute the hard interaction scattering amplitudes in the form of helicity amplitudes, by exploiting a natural equivalence between qubits and helicity spinors. Chapter 5 provides an outline of a Monte Carlo inspired 2-step collinear QCD parton shower on a quantum computer, whilst chapter 6 implements the QCD parton shower in a quantum walk framework which is shown to dramatically increase the performance of the quantum parton shower. The final chapter, 7, discusses possible extensions to provide the next steps to realising a fully quantum simulation of a collision process at the LHC as well as other pertinent avenues to explore applications of QC to HEP in the future.

Chapter 2

Theory and Motivations

2.1 Gauge Theory

The computational framework underpinning the SM is that of Quantum Field Theory (QFT), which is the description of the relativistic elementary particles and their interactions via quantised fields. It is used to accurately describe three of the four fundamental forces (excluding gravity) governing these elementary particle interactions that form the building blocks of the matter that we see before us. These fundamental forces are known as Quantum Electrodynamics (QED), which is the familiar electromagnetic interactions that couples to all charged particles, Quantum Chromodynamics (QCD or the theory of strong interactions) responsible for nuclear binding and the interactions of the constituents of the nuclei, and the theory of weak interactions which is responsible for radioactive decay processes. These fundamental forces collectively dictate the interactions of two types of elementary particles known as fermions, acted on by the fundamental forces, and bosons, which mediate the forces, and are half-integer and integer-spin respectively. A detailed review of QFT and the Standard Model can be found in References [21–23].

The guiding principle of these forces is gauge invariance, where all interactions of nature arise from the requirement of the Lagrangian (theory) to be invariant under a local symmetry transformation.

The fundamental principle of gauge symmetry can be demonstrated by introducing the simple case of gauge invariance in QED [24–26], the theory of electrodynamics, which is an example of an abelian gauge symmetry. This can be generalised to non-trivial field theories, constrained to a gauge symmetry defining theories of multiple vector particles and their interactions with fermions, known as non-abelian gauge theories [27].

First consider a general global phase rotation of a Dirac field ψ given by

$$\psi(x) \rightarrow e^{i\alpha}\psi(x) \tag{2.1.1}$$

where α is the angle of the phase rotation.

The Dirac adjoint of the field defined as,

$$\bar{\psi} = \psi^{\dagger}\gamma^{0}, \tag{2.1.2}$$

undergoes the transformation

$$\bar{\psi} \rightarrow e^{-i\alpha}\bar{\psi}. \tag{2.1.3}$$

Terms formed from bilinears of the Dirac spinors e.g. the mass term

$$m\bar{\psi}\psi \tag{2.1.4}$$

where m is a constant and corresponds to the mass of the Dirac spinor ψ, are invariant under this global phase transformation [1].

However, when promoting an x (space-time) dependence of the α parameter

$$\psi(x) \rightarrow e^{i\alpha(x)}\psi(x) \tag{2.1.5}$$

and demanding a local symmetry, leads to extra terms when kinetic terms involving space-time derivatives are considered. This can be solved, following the procedure

---

[1] The adjoint was necessary to define in order to make the term Lorentz invariant as well as gauge invariant. This is due to the non-unitary nature of the finite dimensional representations of the Lorentz group. More information on Lorentz group representations is discussed in Sec. 2.2

of [23], by considering the derivative of ψ in the direction of the vector η_μ by the limit

$$n^\mu \partial_\mu \psi = \lim_{\epsilon \to 0} \frac{1}{\epsilon} \left[\psi(x + \epsilon n) - \psi(x) \right]. \tag{2.1.6}$$

By introducing a phase factor $U(y, x)$ connecting neighbouring points such that $\psi(y)$ and $U(y, x)\psi(x)$ have the same transformation properties we can define the covariant derivative as

$$n^\mu D_\mu \psi = \lim_{\epsilon \to 0} \frac{1}{\epsilon} \left[\psi(x + \epsilon n) - U(x + \epsilon n, x)\psi(x) \right]. \tag{2.1.7}$$

If the phase is a continuous function of points y and x it can be expanded in the separation of points as

$$U(x + \epsilon n, x) = 1 - ie\epsilon n^\mu A_\mu(x) + \mathcal{O}(\epsilon^2) \tag{2.1.8}$$

Where e is an arbitrary constant and A_μ is a new vector field. This new field is known as the connection, the infinitesimal limit of the comparator of the local symmetry transformations [23].

In this limit the covariant derivative has the form

$$D_\mu \psi(x) = \partial_\mu \psi(x) + ieA_\mu \psi(x) \tag{2.1.9}$$

with the transformation property of A_μ given by the transformation of U in the infinitesimal limit:

$$A_\mu(x) \to A_\mu(x) - \frac{1}{e} \partial_\mu \alpha(x). \tag{2.1.10}$$

This means the covariant derivatives simply transforms the same way as the ψ field as

$$D_\mu \psi(x) \to e^{i\alpha(x)} D_\mu \psi(x), \tag{2.1.11}$$

which allows a way to construct a kinetic term for the fermion field that is also invariant under the transformation.

This results in the familiar form of the Dirac lagrangian in QED for a massive fermion

$$\mathcal{L}_{\text{Dirac}} = \bar{\psi} \left(i \not{D} - m \right) \psi. \tag{2.1.12}$$

A locally invariant kinetic term for A_μ involving its derivatives is given by

$$F_{\mu\nu} = \partial_\mu A_\nu - \partial_\nu A_\mu. \tag{2.1.13}$$

This is known as the electromagnetic field tensor and is also defined by the commutator of covariant derivatives [23]

$$\left[D_\mu, D_\nu \right] = ieF_{\mu\nu}. \tag{2.1.14}$$

The transformation 2.1.5 is known as a U(1) gauge transformation, as the phase rotation corresponds to the U(1) abelian group transformation. By demanding a symmetry of the theory for the Dirac field under this transformation we introduce a four-vector field A_μ, known as the gauge field, that couples to the Dirac field. This physically corresponds to the photon in QED. Hence we obtain the physical theory of electromagnetic interactions from the gauge principle.

Yang and Mills generalised the local phase rotation invariance to theories invariant under non-Abelian groups using SU(2) as an example to explain conservation of nuclear isospin [27]. In quantum mechanics and hence QFT we are interested in these unitary groups that preserve probabilities, acting on a vector space of quantum states.

Transformations under continuously generated groups with group elements that lie infinitesimally close to the identity group element, known as Lie groups, can be written as

$$\psi \left(x \right) \to e^{i\alpha^a(x)t^a} \psi \left(x \right), \tag{2.1.15}$$

where α^a are the infinitesimal group parameters and t^a are Hermitian operators, called the generators of the group. The generators span a vector space of infinitesimal group transformations where the commutation relations

$$[t^a, t^b] = if^{abc}t^c \tag{2.1.16}$$

define the Lie algebra and f^{abc} are called the structure constants.

The U(1) transformation, forming the Abelian group (of phase rotations), is the trivial case which commutes with all other unitary transformations.

A fundamental compact Lie group necessary to formulate the current description of the Standard Model is SU(N), a set of $N \times N$ unitary transformations that satisfy det(U)=1. The generators of SU(N) are represented by $N \times N$ Hermitian matrices where there are $N^2 - 1$ independent generators, t^a.

For SU(N) there are two representations that are of fundamental importance to gauge theory, which are the *fundamental* N-dimensional (D) representation where ψ transforms as an N D complex vector and the *adjoint* representation, in which the generators of the algebra belong. In the adjoint representation, generators are given by the structure constant themselves. The structure constants are real and antisymmetric, conjuring a real representation for the adjoint representation, and the dimension of the representation is given by the number of generators i.e. for SU(N) the adjoint representation is $\left(N^2 - 1\right)$ D. In gauge theory the vector boson fields transforms in the adjoint representation and fermions transform in the fundamental representation.

Field theories formed by considering non-commuting local symmetries are termed non-Abelian gauge theories. In the SM, these are found by requiring invariance under general SU(N) transformations of an N D complex spinor representing the matter field [27]. For these non-Abelian gauge theories, $U(y, x)$ in is now an $N \times N$ dimensional unitary matrix and near $U = 1$ such a matrix can be expanded in terms of Hermitian generators of SU(N). For infinitesimal separation and an arbitrary constant g [23],

$$U(x+\epsilon n, x) = 1 + ig\epsilon n^{\mu} A^a_{\mu} t^a + \mathcal{O}(\epsilon^2). \tag{2.1.17}$$

Inserting this into Eq. (2.1.7) we find

$$D_{\mu} = \partial_{\mu} - igA^a_{\mu} t^a. \tag{2.1.18}$$

Thus, the covariant derivative for an SU(N) local symmetry requires $\left(N^2-1\right)$ vector fields (in correspondence with the number of generators).

Using yet again the infinitesimal transformations, we find the covariant derivative similarly transforms as the fermion field as (to first order in α)

$$D_{\mu}\psi \to \left(1 + i\alpha^a t^a\right) D_{\mu}\psi. \tag{2.1.19}$$

The field strength again determined from the commutator of covariant derivatives gives

$$F^a_{\mu\nu} = \partial_{\mu} A^a_{\nu} - \partial_{\nu} A^a_{\mu} + g f^{abc} A^b_{\mu} A^c_{\nu}, \tag{2.1.20}$$

with an additional term resulting from the non-zero commutator of the generators.

This field strength is no longer gauge invariant but only gauge covariant, and instead a gauge invariant combination is given by the trace

$$\mathcal{L} = -\frac{1}{2}\mathrm{tr}\left[\left(F^a_{\mu\nu} t^a\right)^2\right] = -\frac{1}{4}\left(F^a_{\mu\nu}\right)^2, \tag{2.1.21}$$

which is the gauge invariant kinetic term for A^a_{μ}. There are extra terms in contrast to the Abelian case as it includes non-trivial cubic and quartic interactions and hence this term itself defines a non-trivial interacting field theory known as Yang-Mills theory [27].

Combining this kinetic term with the Dirac Lagrangian we get the non-Abelian Lagrangian,

$$\mathcal{L} = \bar{\psi} \left(i \not{D} - m \right) \psi - \frac{1}{4} \left(F^a_{\mu\nu} \right)^2 . \tag{2.1.22}$$

Further details of the above section can be found in [23].

2.2 Lorentz representations and Weyl spinors

In QFT, the fundamental theoretical description of the theory is the Lagrangian, L, the spatial integral of the Lagrangian density, $\mathcal{L}$, (more conventionally used) which is a function of the relevant fields of the system and their derivatives. In order to respect the Lorentz invariance of the theories, the Lagrangian must be a Lorentz scalar and hence the fields transform under specific Lorentz representations with constrained interactions. Details of the following section, and more information on Weyl spinors can be found in [22]. The Lie algebra of the Lorentz group (LG) known as the Lorentz algebra, $so(1,3)$, can be written as a direct sum of two commuting $su(2)$ sub-algebras i.e.

$$so(1,3) = su(2) \oplus su(2). \tag{2.2.1}$$

Where $su(2)$ is the algebra of Pauli matrices, $\sigma^i, i = 1, 2, 3$ which generates the 3-d rotation group SO(3), and the irreducible representations (irreps) of $su(2)$ are characterised by a half-integer j which acts on a vector space with $2j + 1$ basis elements.

The irreps of the Lorentz group are hence characterised by two half-integers (A, B) with a total of $(2A + 1)(2B + 1)$ degrees of freedom (d.o.f.). The general tensor representations, $T^{\mu_1,\mu_2,..,\mu_n}$, are labelled as $(n/2, n/2)$ representations of the Lorentz algebra. These particles of given spin must be embedded into fields e.g. the Lorentz four-vectors, $A_\mu(x)$, is the $(1/2, 1/2)$ representation that describes spin-1 and spin-0 representations of SO(3). Four-vector fields correspond to the integer spin representations of the Lorentz group, however, another fundamental type of particle in the SM are spin $J = 1/2$ representations of the Lorentz group known as spinors, usually denoted by ψ.

Spinors correspond to the spin-1/2 representations of the LG, of which there are two possible complex representations, $(1/2, 0)$ and $(0, 1/2)$. These are associated with spinors called left-handed (LH) and right-handed (RH) Weyl spinors, denoted ψ_L and ψ_R respectively. These have two d.o.f. each and are defined by the algebra of Pauli matrices i.e. SO(3) algebras. These 2 D Weyl spinors can be combined into the usual Dirac representation within a four-component Dirac spinor as:

$$\psi = \begin{pmatrix} \psi_L \\ \psi_R \end{pmatrix}. \tag{2.2.2}$$

In this representation, the Dirac algebra is used which can also be reduced to the two separate Weyl spinor representations. The Dirac matrices are a set of four, 4×4 matrices given by

$$\gamma^0 = \begin{pmatrix} 0 & \mathbb{I} \\ \mathbb{I} & 0 \end{pmatrix}, \gamma^i = \begin{pmatrix} 0 & \sigma^i \\ -\sigma^i & 0 \end{pmatrix} \tag{2.2.3}$$

which satisfy

$$\{\gamma^\mu, \gamma^\nu\} = 2g^{\mu\nu} \tag{2.2.4}$$

known as the Dirac algebra. This four-vector notation is useful to combine with four-vectors to form Lorentz invariants in the Dirac Lagrangian.

The Dirac spinors are hence reducible and the Weyl spinors, ψ_L and ψ_R, are more fundamental than Dirac spinors because they correspond to irreps of the Lorentz group. However, since theories like QED are symmetric under L↔R interchange it is easier to consider Dirac spinors and instead introduce the γ^5 matrix,

$$\gamma_5 = i\gamma^0\gamma^1\gamma^2\gamma^3, \tag{2.2.5}$$

to define the projectors

$$P_L = \frac{1}{2}\left(1-\gamma_5\right), P_R = \frac{1}{2}\left(1+\gamma_5\right) \tag{2.2.6}$$

to project out the LH and RH Weyl spinors respectively when acted the on Dirac spinors.

These projectors are useful for L↔ R asymmetric theories, such as the theory of weak interactions or for the spinor helicity formalism which will be introduced in chapter 4. In the SM, the four-vector integer-spin fields $A_\mu(x)$ corresponds to the gauge bosons, whilst the half-integer spinors corresponds to the fermions, according the spin-statistics theorem [28–30]. Lorentz invariance and gauge symmetry are thus the guiding principles for the construction of the Lagrangian in QFT.

2.3 The Standard Model

The SM corresponds to the gauge group structure

$$\mathrm{SU}(3)_c \times \mathrm{SU}(2)_L \times \mathrm{U}(1)_Y,$$

[31–37] where $\mathrm{SU}(3)_c$ is the unbroken colour gauge group, QCD [33, 34, 38], which is mediated by vector bosons known as gluons, G^a, where $a = 1, ..., 8$. QCD acts on colour-charged fermions known as quarks, q_c^i, which come in different flavours, i, where $c = 1, 2, 3$ is the colour index. Whilst $\mathrm{SU}(2)_L \times \mathrm{U}(1)_Y$ is the gauge group corresponding to the electroweak (EW) interactions [31, 32, 39], which above the electroweak symmetry breaking scale corresponds to the unification of $\mathrm{SU}(2)_L$ with associated gauge bosons W^i where $i = 1, 2, 3$, with the high-energy hypercharge group $\mathrm{U}(1)_Y$ with associated gauge boson B. The EW gauge group gets spontaneously broken down to the weak $\mathrm{SU}(2)_L$ and electromagnetic gauge group $\mathrm{U}(1)_{EM}$ below the electroweak scale.

Hence, the SM Lagrangian can be split up as [40]

$$\mathcal{L}_{\mathrm{SM}} = \mathcal{L}_{\mathrm{Gauge}} + \mathcal{L}_{\mathrm{Fermion}} + \mathcal{L}_{\mathrm{Higgs}} + \mathcal{L}_{\mathrm{Yukawa}} \tag{2.3.1}$$

Where $\mathcal{L}_{\mathrm{Gauge}}$ denotes the kinetic terms of the gauge fields and is given by

$$\mathcal{L}_{\mathrm{Gauge}} = -\frac{1}{4}G^a_{\mu\nu}G^{a\,\mu\nu} - \frac{1}{4}W^i_{\mu\nu}W^{i\,\mu\nu} - \frac{1}{4}B_{\mu\nu}B^{\mu\nu} \tag{2.3.2}$$

where $G^a_{\mu\nu}$, $W^i_{\mu\nu}$ and $B^{\mu\nu}$correspond to the field strength tensors of the colour, weak, and hypercharge gauge groups, $\mathrm{SU}(3)_c$, $\mathrm{SU}(2)_L$ and $\mathrm{U}(1)_Y$, respectively.

The field strength tensors are given by the following,

$$G^a_{\mu\nu} = \partial_\mu G^a_\nu - \partial_\nu G^a_\mu + g_s f^{abc} G^b_\mu G^c_\nu, \tag{2.3.3}$$

$$W^i_{\mu\nu} = \partial_\mu W^i_\nu - \partial_\nu W^i_\mu + g\epsilon^{ijk} W^j_\mu W^k_\nu, \tag{2.3.4}$$

$$B_{\mu\nu} = \partial_\mu B_\nu - \partial_\nu B_\mu, \tag{2.3.5}$$

where the coupling constants g_s and g are associated with the gauge groups $\mathrm{SU}(3)_c$ and $\mathrm{SU}(2)_L$ respectively and the $\mathrm{U}(1)_Y$ abelian group also has an associated coupling, g'. It can be seen that the non-Abelian gauge group field strength tensors have the additional non-commuting terms leading to self-interactions of the gauge fields.

2.3.1 Fermion sector

As mentioned in Sec. 2.2, the Dirac spinor is formed from the LH and RH Weyl spinors which are associated with the $(1/2, 0)$ and $(0, 1/2)$ irreps of the LG. What is experimentally observed is the chiral nature of the weak interactions (and hence is maximally parity violating) [1] as the W boson couples only to LH relativistic quarks and leptons. Hence the LH fermion fields and RH fields are assigned different representations under the $\mathrm{SU}(2)_L$ gauge group, where LH fields are assigned to the doublet representation of $\mathrm{SU}(2)_L$ whilst the RH field are singlets under $\mathrm{SU}(2)_L$. Therefore, the covariant derivatives for LH and RH components will be different containing two different set of couplings to the gauge bosons. The LH lepton doublets, E^i_L, are formed of the pairs of charged leptons, l^+, with a corresponding neutral neutrino, ν_l, whilst the LH quark doublets, Q^i_L, are formed of up-type quarks with charge +2/3 (u, c, t) and bottom-type ones (d, s, b) with charge -1/3. There are three generations of lepton and quark doublets and are given by the following,

$$E^i_L = \begin{pmatrix} \nu_{eL} \\ e_L \end{pmatrix}, \begin{pmatrix} \nu_{\mu L} \\ \mu_L \end{pmatrix}, \begin{pmatrix} \nu_{\tau L} \\ \tau_L \end{pmatrix} \tag{2.3.6}$$

and

$$Q^i_L = \begin{pmatrix} u_L \\ d_L \end{pmatrix}, \begin{pmatrix} c_L \\ s_L \end{pmatrix}, \begin{pmatrix} t_L \\ b_L \end{pmatrix} \tag{2.3.7}$$

where i runs over the generations i.e. $i = 1, 2, 3$. These pairs of fermion fields that make-up the doublets, transform in the fundamental representation of $\mathrm{SU}(2)_L$ and have isospin values of $T^3 = +(-)\frac{1}{2}$ associated with the up-type (down-type) quarks for the quark doublets, and $T^3 = +(-)\frac{1}{2}$ for the the uncharged neutrino

---

[1] More information on discrete transformations including charge conjugation, time reversal and implications for the SM can be found in [22, 23]

(negatively charged lepton) respectively. The LH quarks have isospin $Y_Q = +1/6$ whilst the leptons have isospin value $Y_l = -1/2$. These hypercharge values have been determined using the relation between electromagnetic charges and assigned isospin values (shown in Eq. (2.3.24) below). Whilst there are six RH quarks, all singlets under $SU(2)_L$ and hence have zero T^3 isospin so that their corresponding hypercharge values are given by the charges of the species. Hence, leading to three (up-type) RH quarks with hypercharge value $Y_u = +2/3$ and three (down-type) with $Y_d = -1/3$ respectively and similarly there are six RH leptons, three charged ones with with $Y_l = -1$ and three neutral neutrinos with $Y_v = 0$. These are shown below

$$e^i_R = \{e_R, \mu_R, \tau_R\}\,, \nu^i_R = \left\{\nu_{eR}, \nu_{\mu R}, \nu_{\tau R}\right\}; u^i_R = \{u_R, c_R, t_R\}\,, d^i_R = \{d_R, s_R, b_R\}\,, \tag{2.3.8}$$

which are also labelled by an index i which runs over the generations. Using all these quantum numbers the form of the covariant derivatives in $\mathcal{L}_{\text{Fermion}}$ (excluding QCD couplings) can be written as the following:

$$D_{\mu,\alpha} = \partial_\mu - igW^i_\mu \tau^i - ig' Y_\alpha B_\mu \tag{2.3.9}$$

where the hypercharge values are determined by the type of particle species, α, with the associated quantum numbers. The fermion Lagrangian consists of the all kinetic terms for all fermionic species which include the covariant derivative and hence interactions of the fermion with the gauge bosons from each respective gauge groups with corresponding charge. For the massless case, this is given by

$$\mathcal{L}_{\text{Fermion}} = \bar{E}_L(i\not{D}_E)E_L + \bar{Q}_L(i\not{D}_Q)Q_L + \bar{u}_R(i\not{D}_u)u_R + \bar{d}_R(i\not{D}_d)d_R + \bar{e}_R(i\not{D}_e)e_R \tag{2.3.10}$$

where each of the covariant derivatives are in the form Eqs. (2.3.9), with their respective hypercharges. The lack of a RH neutrino term will be explained in Sec. 2.3.3.

2.3.2 The Higgs sector

According to the gauge principle, vector bosons that mediate interactions in gauge theories must be massless. Terms like $mA_\mu A^\mu$ for example for the photon field, A_μ, which transforms under Eq. (2.1.10), is forbidden in order to respect gauge invariance. Furthermore, masses of the fermions are also prohibited by gauge invariance in order to to obey the experimentally verified chiral nature of the weak interaction since mass terms mix the LH and RH fields which have different gauge transformations under $SU(2)_L \times U(1)_Y$. This is inconsistent with the experimentally observed masses for fermions as well the heavy vector bosons of the weak interactions: $W^\pm$ and Z. This issue is resolved via the Higgs mechanism [35–37], which is the spontaneous symmetry breaking (SSB) of the local gauge symmetry via the non-zero vacuum expectation value of a complex scalar, which in this case is the Higgs doublet. SSB is a vital mechanism to provide explanation of many crucial aspects of the SM since it is necessary to describe both the theory of weak interactions, as well as strong interactions and may further be used for descriptions of unified models of fundamental physics. The minimum-energy classical energy configuration ϕ_0 of the system found by minimising the potential is known as the vacuum expectation value or vev for short. In the quantum theory, the minimum is used as the ground state to build the excitation of states in the Hilbert space. So SSB occurs when a choice of the vev is made, breaking the vacuum symmetry. For SSB, the Lagrangian is still invariant under the symmetry but the vacuum does not respect the symmetry. Goldstone's theorem [41–43] states that spontaneous breaking of continuous global symmetries implies the existence of massless particles, known as Goldstone bosons, for each broken symmetry generator associated with the vacuum. If the symmetry is gauged, with an associated massless gauge field A_μ, then in the broken phase the gauge bosons associated with the broken generators will acquire a mass, which is known as the Higgs mechanism.

The Higgs mechanism is seen in the Standard Model for non-Abelian gauge theories in the Glashow-Weinberg-Salam model of electroweak symmetry.

The complex Higgs doublet breaks the electroweak gauge structure down to the photon gauge group generating masses for the weak vector bosons while the photon, corresponding to a particular combination of generators, remains massless.

The complex scalar Higgs field, ϕ, transforms in the spinor (doublet) representation of $SU(2)_L$ [23]. This is a complex doublet with hypercharge ½ called the Higgs multiplet. For a ϕ vev of the form

$$\langle\phi\rangle = \frac{1}{\sqrt{2}}\begin{pmatrix} 0 \\ v \end{pmatrix}, \tag{2.3.11}$$

the combination of generators for the following $SU(2)_L \times U(1)_Y$ electroweak transformation

$$\phi \to e^{i\alpha^i \tau^i} e^{i\frac{\beta}{2}} \phi \tag{2.3.12}$$

which leaves this vev invariant is $\alpha^1 = \alpha^2 = 0$, $\alpha^3 = \beta$ which corresponds to the massless photon of the unbroken $U(1)_{EM}$ group.

The Lagrangian for the Higgs boson field including the kinetic and potential terms is given by

$$\mathcal{L}_{\text{Higgs}} = \left|D_\mu \phi\right|^2 + \mu^2 \phi^\dagger \phi - \lambda \left(\phi^\dagger \phi\right)^2, \tag{2.3.13}$$

where the covariant derivative for the Higgs field is given by

$$D_\mu \phi = \left(\partial_\mu - igW^i_\mu \tau^i - i\frac{1}{2}g' B_\mu\right)\phi. \tag{2.3.14}$$

In the unitarity gauge [23] the Higgs multiplet is parametrised as

$$\phi(x) = U(x)\frac{1}{\sqrt{2}}\begin{pmatrix} 0 \\ v + h(x) \end{pmatrix}, \tag{2.3.15}$$

where the spinor has an arbitrary real-valued component given by the sum of the vev, v, and a fluctuating real field with $\langle h(x)\rangle = 0$, and is acted on by a general

SU(2) gauge transformation (which upon acting on the spinor produces a general complex-valued two-component spinor). Using an $SU(2)_L$ gauge transformation to remove $U(x)$ we are left with one real d.o.f. The minimum of the potential occurs for a vev value of

$$v = \left(\frac{\mu^2}{\lambda}\right)^{1/2}, \tag{2.3.16}$$

where after expanding around the vev, the potential takes the form

$$\mathcal{L}_V = -\frac{1}{2}m_h^2 h^2 - \sqrt{\frac{\lambda}{2}} m_h h^3 - \frac{1}{4}\lambda h^4. \tag{2.3.17}$$

This leads to terms of the quantum Higgs boson, a scalar particle with mass

$$m_h = \sqrt{2\lambda} v, \tag{2.3.18}$$

with cubic and quartic self-interaction terms.

The relevant mass terms for the gauge bosons is determined by expanding the field around the vev and isolating the Higgs-gauge boson coupling terms. Using the the explicit form of the $SU(2)_L$ generators, $\tau^i = \frac{\sigma^i}{2}$, we find

$$\Delta\mathcal{L} = \frac{1}{2}\frac{v^2}{4}\left[g^2(W_\mu^1)^2 + g^2(W_\mu^2)^2 + (-gW_\mu^3 + g'B_\mu)^2\right]. \tag{2.3.19}$$

The mass terms are diagonal in a new basis, defined by introducing the gauge fields

$$W_\mu^\pm = \frac{1}{\sqrt{2}}\left(W_\mu^1 \mp iW_\mu^2\right), Z_\mu^0 = \frac{1}{\sqrt{g^2 + g'^2}}\left(gW_\mu^3 - g'B_\mu\right) \tag{2.3.20}$$

with masses

$$m_W = g\frac{v}{2}, m_Z = \sqrt{g^2 + g'^2}\frac{v}{2} \tag{2.3.21}$$

and a massless field

$$A_\mu = \frac{1}{\sqrt{g^2 + g'^2}}\left(g'W_\mu^3 + gB_\mu\right). \tag{2.3.22}$$

The covariant derivative of the Higgs (2.3.14) in terms of the mass eigenstate fields is now

$$D_\mu\phi = \Big(\partial_\mu - i\frac{g}{\sqrt{2}}(W_\mu^+\tau^+ + W_\mu^-\tau^-) - i\frac{1}{\sqrt{g^2+g'^2}}Z_\mu(g^2\tau^3 - g'^2Y)\Big)\phi$$

where

$$\tau^\pm = (\tau^1 \pm i\tau^2). \qquad (2.3.23)$$

It can be seen that the massless gauge boson or photon field, A_μ, couples to the gauge generator

$$Q = T^3 + Y \qquad (2.3.24)$$

which identifies the electric charge:

$$e = \frac{gg'}{\sqrt{g^2+g'^2}}. \qquad (2.3.25)$$

This relation is satisfied by the quantum number assignment determined in Sec. 2.3.1.

The weak mixing angle, θ_W, defines the change of basis between the neutral fields in the mass eigenstates basis and the original $SU(2)_L$,$U(1)_Y$ generator basis, so it can be defined via the relations

$$\cos\theta_w = \frac{g}{\sqrt{g^2+g'^2}}, \sin\theta_w = \frac{g'}{\sqrt{g^2+g'^2}}. \qquad (2.3.26)$$

Re-writing the covariant derivative in terms of these quantities gives

$$D_\mu = \partial_\mu - i\frac{g}{\sqrt{2}}(W_\mu^+\tau^+ + W_\mu^-\tau^-) - i\frac{g}{\cos\theta_w}Z_\mu(\tau^3 - \sin^2\theta_w Q) - ieA_\mu Q, \qquad (2.3.27)$$

where

$$g = \frac{e}{\sin\theta_w}, \qquad (2.3.28)$$

and the masses of the W and Z bosons are related by the following relation

$$m_W = m_Z\cos\theta_w. \qquad (2.3.29)$$

The expansion of the kinetic terms for Higgs around the real scalar field, h, leads to the gauge boson mass terms and the $W^{\pm}$-, Z–Higgs couplings given by

$$\mathcal{L}_K = \frac{1}{2}(\partial_\mu h)^2 + \left[m_W^2 W^{\mu+} W_{\mu-} + \frac{1}{2} m_Z^2 Z_\mu Z^\mu\right] \cdot \left(1 + \frac{h}{v}\right)^2 . \tag{2.3.30}$$

2.3.3 The Yukawa sector

Given the chiral nature of weak interactions, mass terms for fermions of the form $\mathcal{L}_m = -m_f \bar{f} f$, explicitly breaks $SU(2)_L$ symmetry and is therefore forbidden by gauge invariance.

However, electroweak symmetry breaking can generate mass terms for fermions by introducing Yukawa-type interactions between the Higgs and fermions which are gauge invariant under the SM $SU(2) \times U(1)_Y$ electroweak symmetry.

An example of a Yukawa term is for the electron-Higgs coupling given by [1] [22]

$$\Delta\mathcal{L}_e = -\lambda_e \bar{E}_L \cdot \phi \, e_R + \text{h.c.} \tag{2.3.31}$$

which after SSB leads to

$$\Delta\mathcal{L}_e = -\frac{1}{\sqrt{2}} \lambda_e v \bar{e}_L e_R + \text{h.c.} \tag{2.3.32}$$

which is the mass term for the electron whose mass, set by the vev and Yukawa coupling, is given by

$$m_e = \frac{1}{\sqrt{2}} \lambda_e v. \tag{2.3.33}$$

Similar terms can be constructed for the other charged leptons and the down-type quarks. For the remaining fermions (neutrinos and up-type quarks) we require a conjugate Higgs field term, by defining $\tilde{\phi} = i\sigma_2 \phi^*$, which transforms in the fundamental representation of $SU(2)_L$ with hypercharge $-1/2$ [22].

---

[1] h.c. stands for“Hermitian conjugate".

Combining all terms for the quarks, and including possible mixing between generations we can write the Yukawa terms in the simple matrix form,

$$\mathcal{L}^{Q}_{\text{Yukawa}} = -\lambda^{ij}_{d} \bar{Q}^{i}_{L} \cdot \phi \, d^{j}_{R} - \lambda^{ij}_{u} \bar{Q}^{i}_{L} \cdot \tilde{\phi} \, u^{j}_{R} + \text{h.c.} \tag{2.3.34}$$

where $\lambda^{ij}_{u/d}$ are in general complex-valued matrices and after the Higgs acquires a vev, it leads to the mass terms [22]

$$\mathcal{L}^{Q}_{\text{Yukawa}} = -\frac{v}{\sqrt{2}} \lambda^{ij}_{d} \bar{d}^{i}_{L} d^{j}_{R} - \frac{v}{\sqrt{2}} \lambda^{ij}_{u} \bar{u}^{i}_{L} u^{j}_{R} + \text{h.c.}. \tag{2.3.35}$$

Under the operation of CP [23]

$$\lambda^{ij}_{u/d} \to \left(\lambda^{ij}_{u/d}\right)^{*}. \tag{2.3.36}$$

Thus for CP to be a symmetry the matrices would have to be real but with no principle that requires this it appears that Eq. (2.3.34) does maximal violation to all discrete and flavour conservation symmetries. However, the form of the interactions can be simplified using chiral transformations on the quark fields.

To diagonalise the masses, use that there exist two diagonal matrices M_d and M_u and two unitary matrices U_d and U_u where (suppressing the generation indices)

$$\lambda_d {\lambda^{\dagger}}_d = U_d M_d^2 {U^{\dagger}}_d, \; \lambda_u {\lambda^{\dagger}}_u = U_u M_u^2 {U^{\dagger}}_u \tag{2.3.37}$$

and given that $\lambda_d {\lambda^{\dagger}}_d$ and $\lambda_u {\lambda^{\dagger}}_u$ are Hermitian they can be written as

$$\lambda_d = U_d M_d {K^{\dagger}}_d, \lambda_u = U_u M_u {K^{\dagger}}_u \tag{2.3.38}$$

for some two other unitary matrices K_d and K_u.

By freely changing the basis for the RH quarks by $d_R \to K_d d_R$ and $u_R \to K_u u_R$ rotations and the LH quarks by $d_L \to U_d d_L$ and $u_L \to U_u u_L$, this removes the U and

K matrices from the Yukawa terms, leaving diagonal mass matrices M_u and M_d [22]. This is known as going to the mass basis. In the mass basis, the mass terms are

$$\mathcal{L}^{Q}_{\text{mass}} = -\left[m_j^d \bar{d}_L^j d_R^j + m_j^u \bar{u}_L^j u_R^j\right] + \text{h.c.}, \tag{2.3.39}$$

where m_j^d and m_j^u are the diagonal elements of $\frac{v}{\sqrt{2}} M_d$ and $\frac{v}{\sqrt{2}} M_u$ respectively.

The RH field rotations also drop out their kinetic terms since hypercharge interactions are generation diagonal. LH rotations affect the W boson couplings which mix up- and down-type quarks. The LH field rotations do not affect B_μ and W_μ^3 couplings since they only couple same flavour quarks, however, u- and d-type quarks are coupled by the $W^\pm$ interactions and hence affected by the chiral rotations. The weak interaction in the mass basis is thus [22]

$$\mathcal{L}^{\text{W}}_{\text{mass-basis}} = \frac{e}{\sqrt{2}\sin\theta_W}\left[W_\mu^+ \bar{u}_L^i \gamma^\mu (V)^{ij} d_L^j + W_\mu^- \bar{d}_L^i \gamma^\mu (V^\dagger)^{ij} u_L^j\right] + \text{h.c.}, \tag{2.3.40}$$

where $V = U_u^\dagger U_d$ is known as the Cabibbo-Kobayashi-Maskawa (CKM) matrix [44,45] which is a complex unitary 3×3 matrix with nine d.o.f.. However, an additional $U(1)^6$ symmetry allows to take six phase rotations and eliminate five phases leaving four d.o.f. overall: three angles and one phase. These are labelled θ_{12},θ_{23} and θ_{13} corresponding to rotations in ij flavour and a phase δ respectively. The existence of a non-zero phase, δ, in the CKM matrix means it is complex, leading to CP violation which can be detected or observed in decays (e.g. in the kaon system).

For leptons, the Yukawa interactions are also of the form Eq. (2.3.34). However, taking neutrino masses as negligible we can neglect right handed neutrino terms since they are uncharged under the gauge groups. Thus, chiral rotations on on the left handed electrons and neutrinos and only on the right handed electrons completely removes the U matrices and K matrices from the theory (commutes through the weak interactions covariant derivatives unlike for the W boson-quark interactions). This makes the lepton-Yukawa terms generational diagonal and the phases are completely rotated away. Hence, the theory of leptons conserves CP exactly and also conserves the lepton family number for each individual flavour, which is also accurately tested experimentally as there are no known observations of flavour-changing muon decay processes.

2.4 The Parton Shower

The theoretical modelling of collisions of a large number of particles at the hadron colliders like the LHC is an enormous feat due to the complexity of the processes. The use of hadrons, composite particles made of colour-charged partons, complicate the interactions greatly at hadron colliders with respect to their lepton collider counterparts. The incoming hadrons formed from constituent partons have multiple interactions (including soft-interactions related to non-perturbative phenomena).

High-energy hard interactions from an "underlying" event of the initial break-up of the proton and the low energy, non-perturbative hadronisation scale are connected by an evolutionary stage that can be calculated using perturbative QCD. These consist of the multiple radiation of additional partons, forming a cascade or parton shower, evolving down in energy scale towards hadron formation [46]. These numerous processes, such as the radiation of large number of partons with incoming and outgoing partons, are too complex to be calculated via exact methods of Feynman diagrams to capture the realistic effects. Instead these high multiplicity final state parton events are simulated using the fundamental simplification introduced by collinear factorisation [47–49] to instead stochastically evolve the emissions into a simple-step program. These have been generalised into widely used platforms known as Monte Carlo event generators [46, 50], which include Herwig, Pythia and Sherpa [51–53]. These algorithms known as parton shower algorithms have been developed to become state-of-the art tools to accurately capture effects seen at LHC today. For more information on event generation for high-energy collisions at hadron colliders, see [46, 50, 54–56].

2.4.1 Collinear Factorisation

The basic principle behind the parton shower algorithms, is that soft/and or collinear emissions are enhanced and hence should dominate the total hadronic cross sections. Under this assumption, parton showers evolve via collinear emissions where given that the transverse momenta of the emitted parton goes to 0, (its Compton wavelength goes to infinity and hence cannot resolve the underlying process) the additional parton can be factored out from the original process to produce a series of mutually independent coherent emissions known as a parton shower [46].

Consider a final-state parton i that splits into partons j and k, carrying momentum fractions z and $(1-z)$ of parton i respectively. Then according to the factorisation theorem [47–49], in the limit in which j and k are collinear ($\theta \to 0$), the partonic differential cross-section for the $(n+1)$-parton process is given by:

$$\mathrm{d}\hat{\sigma}_{n+1} = \mathrm{d}\hat{\sigma}_n \sum_i \int_{k_{min}}^{k_{max}} \frac{\mathrm{d}\left|\mathbf{k}_T\right|^2}{\left|\mathbf{k}_T\right|^2} \int_{z_{min}}^{z_{max}} \frac{\mathrm{d}z}{z} P_{ji}(z) \tag{2.4.1}$$

where $\mathrm{d}\hat{\sigma}_n$ is the cross section for the n-parton process, k_T is the transverse momentum of parton k with respect to j, and $P_{ji}(z)$ is the corresponding Dokshitzer–Gribov–Lipatov–Altarelli–Parisi (DGLAP) splitting functions [57–59] associated with the splitting $i \to jk$ and where we sum over all possible partons i that can lead to the final state parton j. These DGLAP splitting functions are given by

$$P_{gq}(z) = C_F \left[\frac{1+(1-z)^2}{z}\right], \tag{2.4.2}$$

for a quark splitting into a gluon and quark and [54]

$$P_{gg}(z) = C_A \left[2\frac{1-z}{z} + z(1-z)\right], P_{q\bar{q}}(z) = n_f T_R \left[z^2 + (1-z)^2\right], \tag{2.4.3}$$

for the two particle splitting channels: into two gluons and a quark-antiquark pair respectively.

Here, the splitting kernels have colour-charge coefficient factors C_{ii}, where $C_F =$

$\frac{(N_c^2-1)}{2N_c}$, $C_A = N_c$ and $T_R = 1/2$, and for QCD the number of colours is $N_c = 3$. Eq. (2.4.1) becomes singular as $k_T \to 0$, and is regularised by a lower limit on the transverse momentum cutoff known as the factorisation scale, $k_{min} = \mu_F$, whilst the integrals of the momentum fractions z also have limits depending on the kinematics of the process [1].

Given that cross-sections are related to probabilities, we can interpret the factor,

$$\mathrm{d}\hat{\sigma}_{n+1} = \mathrm{d}\hat{\sigma}_n \sum_i \int_{k_{min}}^{k_{max}} \frac{\mathrm{d}\,|\mathbf{k}_T|^2}{|\mathbf{k}_T|^2} \int_{z_{min}}^{z_{max}} \frac{\mathrm{d}z}{z} P_{ji}(z), \tag{2.4.4}$$

as the probability to emit a parton with momentum fraction z of parton i and transverse momentum $\mathbf{k}_T$. Alternatively, we can also write the above probability by introducing the Lorentz-invariant virtuality $t = p_i^2$ of parton i where for the emission of several partons from parton i, with the virtuality decreasing with each emission, we have what is known as a parton cascade where the parton gets closer to being on-shell so that the final on-shell condition provides a natural cutoff to the virtuality, labelled as t_0 (parton will never be on-shell since free partons do not exist). Defining the probability of emitting partons that are non-resolvable by a physical detector with finite resolution between virtualities (t_0, t_1), labelled $\Delta(t_0, t_1)$, we can write

$$\Delta_i(t_0, t_0 + \delta t) = \Delta_i(t_0, t) \left[1 - \sum_j \int_t^{t+\delta t} \frac{\mathrm{d}t}{t} \int \mathrm{d}z P_{ji}(z) \right]. \tag{2.4.5}$$

This says that the probability that there are no resolvable emissions between virtualities t_0 and $t + \delta t$ can be split up into the product of probabilities of the no-resolvable emissions between the intermediate intervals (t_0, t) and $(t, t + \delta t)$. But Taylor expanding both sides to first order in δt we can obtain a differential equation for $\Delta_i(t_0, t_i)$ to obtain the solution [46]

$$\Delta_i(t_0, t) = \exp\left[-\sum_j \int_{t_0}^{t} \frac{\mathrm{d}t'}{t'} \int_{z_{min}}^{z_{max}} \mathrm{d}z P_{ji}(z) \right], \tag{2.4.6}$$

---

[1] The splitting functions also contains terms (not included) with a divergence in the soft-limit of the emitted parton, i.e. $z \to 1$. However, these can be taken care of with the addition of virtual corrections so that the modified splitting functions contains what are known as **plus distributions** [55]

known as the Sudakov factor. The Sudakov factor is integral to the Monte-Carlo algorithms. A given parton cascade, characterised by a set of values (z_i, t_i) denoting the momentum fraction and virtuality before each branching, can be associated with the probability

$$P^{j_1,j_2,\ldots,j_n}_{i_1,i_2,\ldots,i_n}\left(\{z_i\},\{t_i\}\right) = \left[\prod_{m=1}^{n} \Delta_{i_m}\left(t_m, t_{m+1}\right)\right]\left[\prod_{m=1}^{n} \int \mathrm{d}\tilde{z}_{m+1} P_{i_{m+1} i_m}\left(\tilde{z}_{m+1}\right)\right], \quad (2.4.7)$$

where

$$\tilde{z}_{m+1} = \frac{z_{m+1}}{z_m}$$

is the fraction of the momentum of the m^{th} parton that is carried by parton $(m+1)$.

2.4.2 Monte Carlo Method

Thus we can approximate the multiparton final state cross section by generating sets of numbers (z_i, t_i) weighted by the probability of Eq. (2.4.7), obtaining a list of four-momenta of the final products [55,60]. The parton shower programme starts off with a parton with an initial virtuality, t_1, and momentum fraction, $z_1 = 1$, where the next virtuality t_{i+1} is generated by solving

$$\Delta_i\left(t_{i+1}, t_i\right) = r_1 \quad (2.4.8)$$

where r_1 is random number uniformly distributed on [0, 1]. The process is stopped at any step if $t_{i+1} < t_0$ otherwise, after choosing a species for the parton after branching, a further momentum fraction $\tilde{z}_{m+1}$ is generated by solving

$$\frac{\int^{\tilde{z}_{m+1}} \mathrm{d}z' P_{i_{m+1} i_m}(z')}{\int \mathrm{d}z' P_{i_{m+1} i_m}(z')} = r_2 \quad (2.4.9)$$

where r_2 is another random number uniformly distributed on [0, 1] and an azimuthal angle, ϕ, for the next parton $(m+1)$ is generated uniformly on $[0, 2\pi]$. These steps are repeated for all partons. The above algorithm corresponds to the generation of final state radiation, however initial state radiation can also be generated by evolving backwards from the parton in hard scattering event. Details on initial-state parton showers are given in [55, 60, 61]. There are several other types of advanced parton showers which also account for soft emissions, known as wide-angle soft, for purely soft (non-collinear) radiation [60,61] which are similarly enhanced. These are for non-negligible angles between the final state partons which can therefore interfere with each other. These effects are accounted for in QCD showers using colour coherence (final state partons considered by their net colour charge) by introducing angular ordering. More details on this and other possible procedures like dipole showers can be found in references [60, 62, 63].

Chapter 3

Introduction to Quantum Computing

3.1 Introduction to Quantum Computing

The underpinning principle behind quantum computation (QC) is the use of quantum mechanics to perform computations instead of classical physics. It was thought that by utilising the nature of quantum mechanics, by using features such as entanglement and interference, quantum computers could potentially provide an exponential speedup over classical algorithms.

These speculations were justified by two major breakthroughs in quantum computational theory, in 1994 by Peter Shor, who constructed quantum algorithms to tackle two significant problems – the problem of finding the prime factors of an integer and the so-called ‘discrete logarithm’ problem [64]. These were demonstrated to have an efficient solution on a quantum computer which otherwise were widely believed to have no efficient solution on a classical computer.

The computational advantage of QC was further exhibited via Grover’s algorithm [65], a quantum search algorithm devised by Lov Grover in 1995, which could search through some unstructured database for a solution and provided a quadratic speedup over known classical algorithms.

Apart from attaining a speedup over existing classical algorithms, a natural motivation for QC suggested by Feynman in 1982, was use of quantum mechanics to simulate quantum systems. This was due to the inherent difficulties in simulating quantum mechanical systems on classical computers whilst QC's were expected to simulate the highly entangled structures and exponentially large Hilbert spaces of quantum systems more efficiently [66–68]. These wide-ranging applications, from improvements on existing algorithms to developing algorithms for unexplored quantum regimes or systems, would have profound implications for scientific development and technology.

3.1.1 The Qubit

The *bit* is the fundamental unit of classical computation and information, whilst quantum computation and information is built on the *qubit*. Whilst the classical bit is a state that takes the binary value 0 or 1, the qubit is mathematically defined as a two-dimensional complex vector that belongs to a Hilbert space formed from two analogous states, denoted $|0\rangle$ and $|1\rangle$, which form an an orthonormal basis for the 2 D complex Hilbert space.

Since these major theoretical developments, there have been great efforts to build quantum information processing systems where many techniques for controlling single quantum systems have been developed [1]. The qubit which is realised physically as a two-level quantum system has various experimental implementations including: the two different polarisations of a photon; the alignment of a nuclear spin in a uniform magnetic field and the two states of an electron orbiting a single atom (where the orbiting electron exists in either the 'ground' or 'excited' state corresponding to $|0\rangle$ and $|1\rangle$). There has been rapid progress in the development of quantum hardware with only recently in December 2023, IBM unveiling a quantum gate computer called "Condor" with over 1000 qubits [69]. However, in the current NISQ-era there remains publicly accessible QC's of only a few-100's of qubits in size, so that developing resource-efficient quantum algorithms will be prove to be crucial for any short-term implementations for proof-of-principle demonstrations for future fault-tolerant quantum computation.

The qubit state as previously described is given in terms of two orthonormal basis states, $|0\rangle$ and $|1\rangle$, but unlike the classical bit the general qubit state can be given as a linear combination of these basis states known as superposition in quantum mechanics

$$|\psi\rangle = \alpha|0\rangle + \beta|1\rangle, \tag{3.1.1}$$

where α and β are complex numbers and the probability of obtaining a $|0\rangle$ or $|1\rangle$ state on measurement is given by $|\alpha|^2$ and $|\beta|^2$ respectively. The probabilities must sum to 1 leading to normalisation requirement of 1 for the qubit state, making it a unit vector in a 2- d complex vector space. A convenient geometric representation of the qubit state is given by using the $|\alpha|^2 + |\beta|^2 = 1$ requirement to rewrite equation Eq. (3.1.1) as

$$|\psi\rangle = e^{i\gamma}\left(\cos\frac{\theta}{2}|0\rangle + e^{i\phi}\sin\frac{\theta}{2}|1\rangle\right) \tag{3.1.2}$$

where θ, ϕ and γ are real numbers. Ignoring the factor of $e^{i\gamma}$ out the front since it has no observable effects on overall probabilities, we can effectively write

$$|\psi\rangle = \cos\frac{\theta}{2}|0\rangle + e^{i\phi}\sin\frac{\theta}{2}|1\rangle \tag{3.1.3}$$

where the numbers $0 \leq \theta \leq \pi$ and $0 \leq \phi \leq 2\pi$ define a point on the unit three-dimensional sphere known as the Bloch sphere [1]. The Bloch sphere, as shown in Fig. 3.1, provides a useful visualisation of the qubit state, where operations on a single qubit state can also be represented on the Bloch sphere. Given the continuous nature of the θ and ϕ variables, there are an infinite number of points on the unit sphere that can be described by the single qubit stored in the amplitudes of the computational basis states. However, a measurement of the wave function collapses the state onto one of the computational basis states and so practically infinitely many measurements would be needed on identically prepared states to determine α and β for a qubit. Regardless, this huge amount of 'hidden' information along with the fundamental quantum mechanical properties of interference will prove to be a vital asset to exploit the computational power of quantum computing.

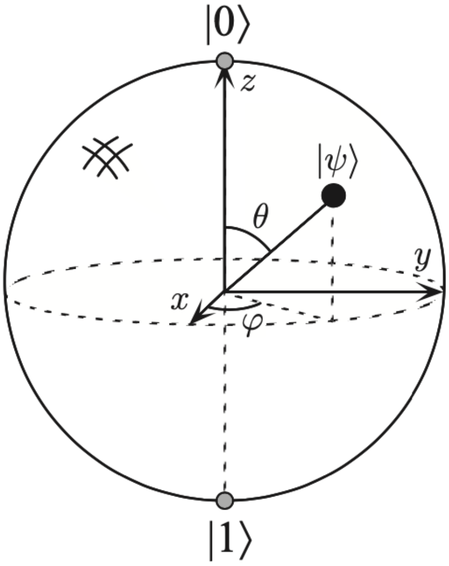

Figure 3.1: Visualisation of the Bloch sphere representation of the qubit, taken from [1].

3.1.2 Multi-Qubit entanglement

A crucial feature for taking full advantage of QC is quantum entanglement, which can be introduced by considering multiple qubit states. A key demonstration of this is the creation of the EPR bell states, named after Einstein, Rosen and Podolsky, who in 1935 considered the famous thought experiment whose implications would pose a serious challenge to existing physical laws according to relativity [70]. The premise of the thought experiment is a two-qubit quantum system. For a two-qubit system, there are four computational basis states denoted $|00\rangle$, $|01\rangle$, $|10\rangle$ and $|11\rangle$. The Bell state or EPR pair is given by

$$\frac{1}{\sqrt{2}}\left(|00\rangle+|11\rangle\right). \tag{3.1.4}$$

Once this state is prepared, we imagine the first qubit belonging to a system A at a given position whilst the second qubit belonging to system B at some location at an arbitrary distance away. The Bell state has the property that upon measuring the first qubit (in system A), one obtains two possible results: 0 with probability 1/2, leaving the post-measurement state $|\phi'\rangle = |00\rangle$, and 1 with probability 1/2, leaving $|\phi'\rangle = |11\rangle$. As a result, a measurement of the second qubit always gives the same result as the measurement of the first qubit. That is, the measurement outcomes are correlated i.e. the two system qubits are entangled. These correlations became an important centre-point of discussion and heavy debate where Einstein, Podolsky and Rosen, believed that this instantaneous communication between the two qubit states belonging to two systems would suggest communication between systems that would exceed the speed of light, c, and violate relativity [70]. To resolve this, they proposed an explanation under the name of the local hidden-variable theory where the outcomes are actually predetermined by some 'hidden' parameter. The expectations of these theories were quantified by John Bell in 1964 who defined the Bell inequalities which predicted the expectation of the correlation between the measurements under the constraints according the local hidden-variable theory [71]. It was soon found that these inequalities were violated by multiple experiments, where the recent 2022 Nobel Prize in physics was in fact awarded for experiments conducted by Alain Aspect, John Clauser, and Anton Zeilinger whose results proved a violation of Bell's inequalities and were consistent with an inherent quantum mechanical explanation rather than a local hidden-variable theory [72–76].

3.1.3 Quantum Gates and Circuits

A computation in a quantum computer is represented by a quantum circuit, built from wires and gates as in the classical case but with the wires usually representing a time direction from left to right, where a wire is displayed for each individual qubit in the quantum circuit and the gates are quantum operators applied to manipulate the quantum state.

The quantum gates operations act linearly on the qubit state, and the application of consecutive gate operations correspond mathematically to the multiplication of the matrix representations acting on the initial state vector. Transformed states must still satisfy the unit-one normalisation condition leading to all operations being unitary and hence making the entire computation in principle reversible, unlike in classical computations. Crucial basic gates used in quantum computation are the X,(known as NOT) Y and Z gates, given by the Pauli matrices. The X gate simply changes the $|0\rangle$ state to a $|1\rangle$ state and vice versa (exchanges the computational basis states). Given the Hermitian nature of the Pauli matrices, application of the gates twice undoes the transformation i.e. for e.g the NOT gate, $XX = XX^\dagger = \mathbb{I}$, where $X^\dagger$ is the adjoint of the X matrix. The Z gate leaves $|0\rangle$ unchanged and flips the sign of $|1\rangle$ to give $-|1\rangle$, and the Hadamard gate, H, when applied to the computational basis states forms a linear superposition of them where it is given by

$$H = \frac{1}{\sqrt{2}} \begin{pmatrix} 1 & 1 \\ 1 & -1 \end{pmatrix}. \tag{3.1.5}$$

These single qubit gates correspond to rotations and reflections of the state on the Bloch sphere. The Hadamard operation is just a rotation of the sphere about the y-axis by 90°, followed by a rotation about the x-axis by 180°. An arbitrary single qubit unitary gate can be decomposed as a product of rotations together with a (global) phase shift [1] i.e.

$$U = e^{i\alpha} \begin{pmatrix} e^{-i\frac{\beta}{2}} & 0 \\ 0 & e^{i\frac{\beta}{2}} \end{pmatrix} \begin{pmatrix} \cos\frac{\gamma}{2} & -\sin\frac{\gamma}{2} \\ \sin\frac{\gamma}{2} & cos\frac{\gamma}{2} \end{pmatrix} \begin{pmatrix} e^{-i\frac{\delta}{2}} & 0 \\ 0 & e^{i\frac{\delta}{2}} \end{pmatrix} \tag{3.1.6}$$

where α, β, γ, and δ are real-valued. A useful property in quantum computing, is that it is possible to build up an arbitrary single qubit gate using a finite set of quantum gates corresponding to special fixed values of α, β and γ. This corresponds to the universality of QC and is guaranteed under what is called the Solovay-Kitaev theorem [1]. However, in order to generate a universal set it must be possible to generate entanglement, a gate that does this and a crucial component in quantum algorithms is the controlled-NOT or CNOT gate. This gate has two input qubits, known as the control qubit and the target qubit, respectively. The circuit representation given by a black circle to represent the control qubit, and an empty circle for the target. The action of the gate is such that if the control qubit is in the $|1\rangle$ state it applies a NOT gate to the target and otherwise left alone. The action of the gate may be summarised as follows:

$$|A, B\rangle \rightarrow |A, B \oplus A\rangle, \tag{3.1.7}$$

where $\oplus$ is addition modulo two.

An example of a quantum circuit is the preparation of the Bell state which is formed by applying a Hadamard gate to qubit 1 and applying a CNOT controlled from qubit 1 applied to target qubit 2 i.e.

$$|00\rangle \overset{H}{\rightarrow}= \frac{1}{\sqrt{2}}\left(|00\rangle + |10\rangle\right) \overset{CNOT}{\rightarrow}= \frac{1}{\sqrt{2}}\left(|00\rangle + |11\rangle\right) \tag{3.1.8}$$

This is depicted in Fig. 3.2

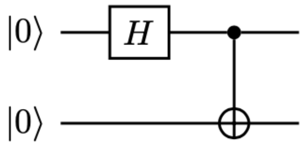

Figure 3.2: Circuit diagram for the preparation of the Bell pair state.

A breakdown of the basic circuit gates, described and their circuit and matrix representations are outlined in Appendix A.1. We see that a system of n qubits states, with computational basis states of the form, $|x_1 x_2 ... x_n\rangle$, is specified by 2^n amplitudes. This idea that the Hilbert space grows exponentially with system size means manipulating and storing information for these systems would be inconceivable for a classical computer whilst possible with a QC. This natural storage and computation associated with exponentially large Hilbert spaces provides a tantalising prospect for the use of QC for more complicated and larger quantum systems which are currently unexplored on classical computers. These include molecular chemical systems as well as real-time simulations in high-energy physics, where the large degrees of freedom and intrinsic entangled structure of the physical systems would be captured by a quantum system. This could provide completely newfound insights into unexplored regimes of physics.

3.2 The Quantum Walk

The design and development of quantum algorithms have been motivated to solve problems more efficiently than their classical counterparts. An example of a classical algorithm which has been vital as a calculational tool with applications to various branches in science and information theory, is the classical random walk [77]. This has sparked similar interest in their quantum analogue, the Quantum random walk otherwise shortly known as quantum walk (QW), which is expected to have the same importance as a powerful algorithmic tool in quantum information science and computation. The classical random walk [77] can be intuitively explained by considering the simplest case of a random walk on an integer number line where the particle begins in position space at 0, and moves either left and right with equal probability 1/2 at a given step. It is known that the in the limit of large number of steps, the probability distribution reaches a Gaussian distribution centred around 0 with a variance of $\sigma^2 = N$, where N is the number of steps.

In the quantum case the QW takes place in a Hilbert space where the two major models are known as continuous-time and discrete-time quantum walks [78,79]. Both walks have a position Hilbert space, $\mathcal{H}_P$, spanned by the position basis states of the particle, however, the discrete-time QW has an additional coin Hilbert space, $\mathcal{H}_C$, used to define the directions that the particle can move in [79–82]. The discrete-time QW is the focus of the following work in this thesis, discussed in chapter 6. The total Hilbert space of a discrete-time QW is denoted as

$$\mathcal{H} = \mathcal{H}_C \otimes \mathcal{H}_P. \tag{3.2.1}$$

Considering the discrete-time QW on a 1 D line, the coin Hilbert space of dimension two is spanned by the basis (internal) states of the particle, $|0\rangle$ and $|1\rangle$, which represent the directions left and right respectively. The position Hilbert space is spanned by the basis states of the position $|j\rangle$, where $j \in \mathbb{Z}$ (where for finite dimensional position space and finite steps N, we consider the range $\{-N, N\}$ instead). Analogous to the classical case, there is a "coin-flip", C, in the coin space, performed as a unitary transformation on the coin Hilbert space, which defines the direction in which the particle moves along with a subsequent position shift operation, S, controlling from coin space to implement the direction of movement of the particle in position space. The entire operation can be represented for a given step as

$$U = S \cdot (C \otimes \mathbb{I}), \tag{3.2.2}$$

where $\mathbb{I}$ is the identity operator in $\mathcal{H}_P$ and the shift operation (controlling from state of the coin) is given by

$$S = |0\rangle\langle 0| \otimes \sum_{i=-\infty}^{\infty} |i-1\rangle\langle i| + |1\rangle\langle 1| \otimes \sum_{i=-\infty}^{\infty} |i+1\rangle\langle i|. \tag{3.2.3}$$

The classical random walk can be replicated by using a coin operation which puts the coin space in an equal superposition of basis states $|0\rangle$ and $|1\rangle$ so that there is equal probability of moving left and right. Such a coin is given by the Hadamard operator which upon acting on a $|0\rangle$ state gives

$$C|0\rangle = H|0\rangle = \frac{1}{\sqrt{2}} \left(|0\rangle + |1\rangle\right). \tag{3.2.4}$$

Such a walk with a Hadamard coin operation is called a Hadamard walk. The following shift operation then places the walker into a superposition of $|1\rangle$ and $|-1\rangle$

position states as shown by

$$U|0\rangle \otimes |0\rangle = \frac{1}{\sqrt{2}} \left(|0\rangle \otimes |i = -1\rangle + |1\rangle \otimes |i = +1\rangle \right). \tag{3.2.5}$$

After this single step, upon measurement of the particle (in the coin register) there is an equal probability of finding the walker in the $|1\rangle$ and $|-1\rangle$ position states as in the classical case [77]. Repeating this procedure of applying the Hadamard operation then shift and measurement at each step, a Gaussian distribution is obtained in the limit of large number of steps [80]. However, the quantum case is given by iterating the steps without measurement, leading to correlations between different position states being maintained due to interference of the left-moving and right-moving amplitudes leading to a drastically different distribution. This results in a quadratic growth of variance with the number of steps in comparison to the classical case where the variance is now given by $\sigma^2 = N^2$ [83–85].

An example simulation of the Hadamard walk for N=100 steps for the 1 D discrete-time QW is shown in Fig. 3.3 and compared to the classical case (quantum with measurement at each step). For the total of N=100 even steps the odd positions by default will have zero probabilities associated with it and the zero-valued probabilities have been removed from the distributions. The Gaussian distribution for the classical case centered around 0 is displayed as expected, whilst stark distinction in the quantum case is seen. The figure shows the distribution for an initialised state in a symmetric superposition of the coin basis states i.e. $\frac{1}{\sqrt{2}} \left(|0\rangle + i|1\rangle \right)$. However, asymmetry can be introduced for an initialised state of either $|0\rangle$ or $|1\rangle$ where for an initialised state of $|0\rangle$ in the coin space, the distribution would be skewed to the left whilst for an initial state $|1\rangle$, the opposite direction of skewness would be observed towards the right. This can be attributed to the difference in the treatment of the $|0\rangle$ (left-moving) and $|1\rangle$ (right moving) internal basis states of the coin space by the Hadamard operator which introduces an extra negative sign on the $|1\rangle$ when acted

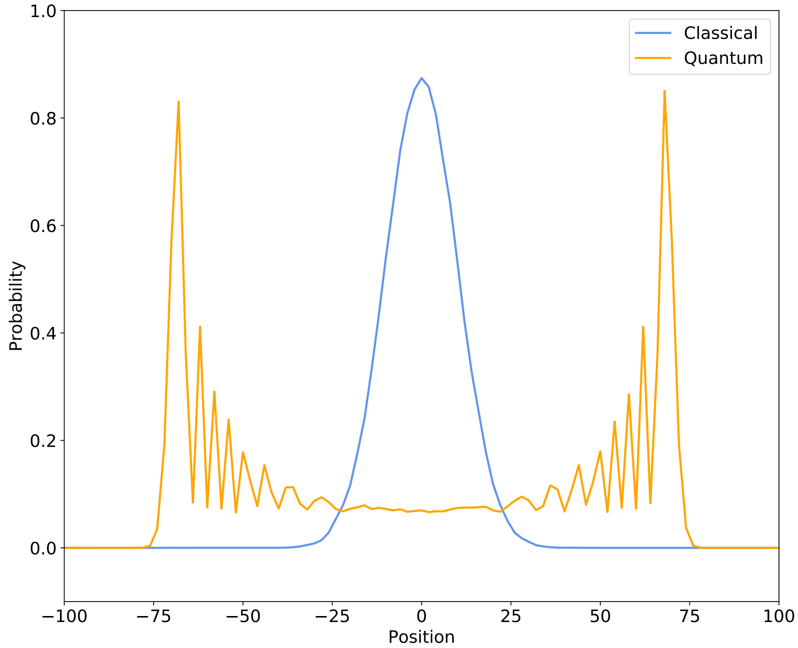

Figure 3.3: Simulation of a 100-step random walk using the IBM Q 32-qubit simulator [2] for 100,000 shots for a classical random walk obtained by measuring the coin state after each step, and a quantum random walk using a symmetric initial state and a Hadamard coin (taken from [3]).

on the $|1\rangle$ state as shown below:

$$H|1\rangle = \frac{1}{\sqrt{2}}\left(|0\rangle - |1\rangle\right). \tag{3.2.6}$$

This leads to more cancellations with the right-moving amplitude when initialised in the $|0\rangle$ state i.e. constructive interference towards the left (and destructive towards the right) and the opposite when acted on the $|1\rangle$ state. This is demonstrated by considering the analytical calculation of the first three steps after application of the U operator.

When acted on the $|0\rangle$ coin state this gives

$$\begin{aligned} |0\rangle \otimes |0\rangle &\xrightarrow{U} \frac{1}{\sqrt{2}}\left(|0\rangle \otimes |-1\rangle + |1\rangle \otimes |1\rangle\right) && (3.2.7) \\ &\xrightarrow{U} \frac{1}{2}\left(|0\rangle \otimes |-2\rangle + (|0\rangle + |1\rangle) \otimes |0\rangle\right) - |1\rangle \otimes |2\rangle && (3.2.8) \end{aligned}$$

$$\xrightarrow{U} \frac{1}{2\sqrt{2}}\left(|0\rangle \otimes |-3\rangle + (2|0\rangle + |1\rangle) \otimes |-1\rangle - |0\rangle \otimes |1\rangle + |1\rangle \otimes |3\rangle\right) \tag{3.2.9}$$

Whilst when acting on the $|1\rangle$ coin state this leads to

$$|1\rangle \otimes |0\rangle \xrightarrow{U} \frac{1}{\sqrt{2}}\left(|0\rangle \otimes |-1\rangle + |1\rangle \otimes |1\rangle\right) \tag{3.2.10}$$

$$\xrightarrow{U} \frac{1}{2}\left(|0\rangle \otimes |-2\rangle + (|1\rangle - |0\rangle) \otimes |0\rangle\right) + |1\rangle \otimes |2\rangle \tag{3.2.11}$$

$$\xrightarrow{U} \frac{1}{2\sqrt{2}}\left(|0\rangle \otimes |-3\rangle + |1\rangle \otimes |-1\rangle + (|0\rangle - 2|1\rangle) \otimes |1\rangle\right) - |1\rangle \otimes |3\rangle \tag{3.2.12}$$

demonstrating the asymmetry of probabilities described. The quadratic speedup for the quantum walker has motivated for further considerations of quantum advantages over the classical case, where numerous examples have already been proven for quantum walks. For example the exponential speedup over classical computation for a hitting time problem on a glued tree and more interestingly, it has also been shown to achieve quantum advantage for certain cases such as search algorithms [86, 87] and simulated annealing [88, 89], both based on Markov Chain Monte Carlo (MCMC). MCMC being central to modern computational science, including forming the basis of parton shower algorithms in HEP, motivates its potential use as a natural framework for physical processes in HEP and forms the major theme of chapter 6, where we introduce the novel idea by applying a quantum walk algorithm to simulate the parton shower process.

Chapter 4

Helicity Amplitudes on a Quantum Computer

4.1 Motivations

The unique advantages offered by quantum computing including, features such as quantum interference, superposition and entanglement, is believed to provide a more accurate computational framework for the simulation of quantum mechanical processes including high-energy processes. QC has already been proven to demonstrate clear advantages over classical algorithms [64, 65]. One key application where QC is expected to provide a unique advantage is in the simulation of lattice field theories to describe non-perturbative physics. Lattice QCD (LQCD) has been very successful, enabling the computation of quark masses, running of the coupling, masses of QCD bound states, and the structure of hadrons. However, despite the successes of using Monte Carlo (MC) methods in LQCD, a major inherent limitation is the inability for real-time simulation in Minkowski space-time. Connected to this is the fundamental “sign problem”: theories with a non-zero chemical potential or with topological terms (e.g. QCD with the CP-violating θ-term) are not amenable to MC methods as they lead to an imaginary contribution to the Euclidean action. QC can help bypass this issue with the use of direct Hamiltonian simulation in quantum computing systems [90, 91]. However, in the current era of NISQ-devices full quantum simulations of lattice field theories remain untenable and instead we focus in this thesis on enhancing or introducing new features to existing classical algorithms by shifting to the quantum paradigm.

In this chapter we will elucidate how the calculation of a hard process in terms of helicity amplitudes can be performed using a Gate Quantum Computer (GQC) as demonstrated in [4]. First we will introduce the spinor helicity formalism in Sec. 4.2 and then demonstrate the equivalence of the helicity spinor and qubit in section Sec. 4.3. We will then outline ways to initialise these spinors using quantum unitary gates on a QC in Sec. 4.3.1. For proof of concept, helicity amplitudes for a 1 → 2 process and a 2 → 2 quark gluon scattering process are demonstrated in Sec. 4.3.2 and Sec. 4.3.3 respectively, for which the results are compared to the classical amplitudes.

4.2 Spinor Helicity formalism

The simulations of high-energy collisions in colliders like the LHC involve the production of a large number of energetic partons, which evolve to events with many jets in the final state. Simulating the Standard Model prediction of these events, known as background, to LHC simulation processes is crucial to potentially discovering new physics with many multi-jet final process providing a probe to these and setting limits of numerous phenomenological extension models known as BSM models. While branching probabilities describe parton evolution under the assumption of collinear and soft emissions and are effectively modelled using Monte Carlo techniques as mentioned in Sec. 2.4.2, to a good approximation it fails to capture emissions with large relative transverse momentum, for which a full calculation of the matrix elements for the these hard processes involving many partons is required.

In the usual Feynman diagram approach to calculating amplitudes, a perturbative series expansion in order of couplings associated with the theory where all possible diagram processes contributing to the scattering process at a given order is considered. Higher order terms are given by increasing number of closed loops on the diagrams. Diagrams are constructed according to the all possible processes given by the set of interactions of the particles determined by the Lagrangian of the theory with amplitudes computed using the corresponding Feynman rules.

However, calculating scattering cross section using the Feynman diagram techniques for increasing number of particles becomes exceedingly complex. These effects are even more pronounced in QCD, which is necessary to simulate hadronic collisions, where the self-coupling of the gluon leads to a proliferation in the number of diagrams even at tree level. It is known for example that the scattering process for $gg \to 8g$ requires more than one million diagrams, which is evidently impossible to compute. However, it has been found that significant simplifications are introduced in these calculations by introducing what is known as the spinor helicity formalism which forms the basis of this chapter. The formalism has lead to the discoveries of numerous useful results to simplify large parton calculations in QCD via the use of recursive methods, used to compute multi-gluon scattering amplitudes in QCD. Unlike in Feynman diagrams, the individual amplitudes known as helicity amplitudes are gauge-invariant as amplitudes are taken to be on-shell. This means amplitudes can be individually squared then summed, alternatively to having to sum and square over all possible Feynman diagrams in order to make the gauge invariant sums "physical". All these utilities provide motivation for the use of helicity amplitudes to aid future LHC simulations with it already having been integrated in packages in MC event generators for hard matrix element calculations and having been shown to improve the theoretical description of scattering events [56]. The fundamental idea underpinning the spinor helicity formalism is that momenta, usually represented in four-vector notation as, p^μ, transforms under the $(\frac{1}{2}, \frac{1}{2})$ representation of the LG (as seen in Sec. 2.2) and hence are more naturally described by bispinors, $P_{\alpha\dot{\alpha}}$, where like the Weyl spinors the α index is associated with the LH $(\frac{1}{2}, 0)$ representation and the $\dot{\alpha}$ index with the RH $(0, \frac{1}{2})$ representation. Helicity spinors solve the massless

Dirac equation with two independent solutions associated with the Dirac spinors of the outgoing anti-fermion and fermion respectively, shown in Appendix B.1, and where the incoming ones can be determined from crossing symmetry. The two-component commuting spinors correspond to the LH and RH Weyl spinors in Sec. 2.2 and are written in terms of angle and square Dirac bra and ket notation. Where again the undotted, α, indexed spinors correspond to the LH spinors and the dotted, $\dot{\alpha}$, to the RH spinors and square belonging to the positive helicity and angle to the negative helicity ones. Under these conventions and the bispinor form of momenta, calculations are massively simplified. Since the LH and RH components are decoupled, the two-component spinors will be directly used instead of the four-dimensional Dirac ones, although the correspondence between the two is found in Appendix B.1.

4.3 Helicity Spinors and Qubits

As defined in Sec. 4.2, Helicity spinors are defined as 2 D complex Weyl spinors that solve the massless Weyl equation.

The motivation for the computation of helicity amplitude on a GQC follows from considering the parametrisation of the four-momentum vector of a particle with energy E as [92]

$$p^{\mu} = (E, E\sin\theta\cos\phi, E\sin\theta\sin\phi, E\cos\theta) \tag{4.3.1}$$

in terms the angular variables θ and ϕ and where $p^{\mu}p_{\mu} = 0$ (for massless case) using the $\eta_{\mu\nu} = \mathrm{diag}(-1, +1, +1, +1)$ metric convention. The following corresponding helicity spinor associated with it is given by

$$|p\rangle^{\dot{a}} = \sqrt{2E}\begin{pmatrix} \cos\frac{\theta}{2} \\ \sin\frac{\theta}{2}e^{i\phi} \end{pmatrix} \tag{4.3.2}$$

where the other spinors $\langle p|_{\dot{a}}$, $|p]_{a}$ and $[p|^{a}$ are related by two bispinor momenta matrices, $p_{a\dot{b}} = -|p]_a\langle p|_{\dot{b}}$ and $p^{\dot{a}b} = -|p\rangle^{\dot{a}}[p|^b$, outlined in Appendix B.1.

Similarly, as shown in Sec. 3.1.1 the state of the qubit is defined on a 2 D complex vector space with states $|0\rangle$ and $|1\rangle$ forming the orthonormal basis for this space. A general qubit, formed by a linear superposition of these orthonormal basis states can also be parametrised by two angles as seen in Eq. (3.1.3).

$$|\psi\rangle = \cos\frac{\theta}{2}|0\rangle + e^{i\phi}\sin\frac{\theta}{2}|1\rangle = \begin{pmatrix} \cos\frac{\theta}{2} \\ \sin\frac{\theta}{2}e^{i\phi} \end{pmatrix}, \tag{4.3.3}$$

where we can represent the qubit on a three-dimensional unit sphere called the Bloch sphere. The equivalence between these two representations of the qubit and helicity spinor is seen, modulo an overall normalisation factor $2E$. Hence, the calculation of helicity amplitudes can be thought to be constructed by initialising the helicity spinor on a qubit where the θ and ϕ variables of the qubit which parametrises the position on the Bloch Sphere, correspond to the θ and ϕ values of the helicity spinor. Hence, performing unitary quantum operations to manipulate the helicity spinor corresponds to rotations of the qubit state on the Bloch sphere. As a result, the helicity spinor is a faithful representation of the object the circuit directly operates on. The direct correspondence between helicity spinors and qubit states show that GQCs provide an ideal framework for the calculation of helicity amplitudes. This natural framework for helicity calculations is further evidenced by the probabilistic outputs from a quantum algorithm, computed in a quantum algorithm by projecting out the final state and taking iterated measurements. This coincides with intrinsic probabilistic nature of quantum mechanical high energy processes where cross sections are determined from the amplitudes of scattering events. The helicity spinors $|p\rangle^{\dot{a}}$,$(\langle p|_{\dot{a}})^{\mathrm{T}}$, $|p]_a$ and $([p|^a)^{\mathrm{T}}$ are visualised for $\theta = \pi/4$, $\phi = \pi/2$, $E = 1/2$, as vectors on the Bloch sphere in Fig. 4.1, in direct analogy to their respective qubit representation.

Below I outline the basic building blocks to encode spinor helicity calculations on a quantum circuit. In Secs. 4.3.2 and 4.3.3 , it is demonstrated how these basic building blocks are used to construct quantum algorithms for two simple examples of helicity

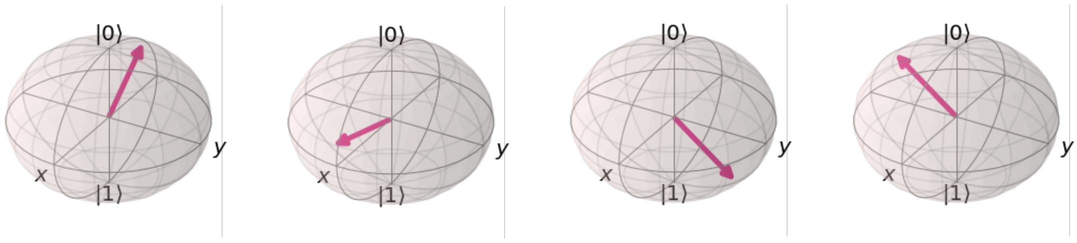

(a) $|p\rangle^{\dot{a}}$ (b) $|p]_a$ (c) $(\langle p|_{\dot{a}})^{\mathrm{T}}$ (d) $([p|^{a})^{\mathrm{T}}$

Figure 4.1: A visualisation of the helicity spinors $|p\rangle^{\dot{a}}$,$|p]_a$, $(\langle p|_{\dot{a}})^{\mathrm{T}}$ and $([p|^{a})^{\mathrm{T}}$ for $\theta = \pi/4$, $\phi = \pi/2$, $E = 1/2$ on the Bloch sphere, following the choice of representation of Eq. (4.3.2) (taken from Reference [4]).

calculations: (i) the contraction of an external polarisation vector corresponding to a $g \to q\bar{q}$ vertex, and (ii) the construction of s- and t-channel amplitudes for a $q\bar{q} \to q\bar{q}$ process with identical initial and final quark flavours. A fundamental concept of "Helicity registers" are crucially introduced into these quantum circuits to control the helicity of each particle involved. In addition, by applying Hadamard gates to the helicity registers, we introduce a superposition state between the helicity qubits of $|0\rangle$ and $|1\rangle$ so that calculations for both helicities of each particle involved can be computed simultaneously, fully utilising the quantum nature of the computation. This advantage is further demonstrated by the simultaneous computation of s- and t-channel amplitudes for the $q\bar{q} \to q\bar{q}$ process.

4.3.1 Constructing helicity spinors and scalar products on the Bloch sphere

The helicity spinors have been implemented on the quantum circuit by utilising the general single-qubit 2 D unitary gate, $U_3(\theta, \phi, \lambda)$, which in qiskit is defined as

$$U_3(\theta, \phi, \lambda) = \begin{pmatrix} \cos\left(\frac{\theta}{2}\right) & -e^{i\lambda}\sin\left(\frac{\theta}{2}\right) \\ e^{i\phi}\sin\left(\frac{\theta}{2}\right) & e^{i(\phi+\lambda)}\cos\left(\frac{\theta}{2}\right) \end{pmatrix}. \tag{4.3.4}$$

Simply acting with a U_3 gate, on a default $|0\rangle$ qubit state produces the $|p\rangle^{\dot{a}}$ spinor where θ and ϕ variables of the $U3$ gate correspond to the θ and ϕ variables of the helicity spinor and λ remains arbitrary. The $|q\rangle^{\dot{a}}$ spinor has been created by sequentially applying a $U_3^\dagger$ rotation and a NOT gate, where here the θ and λ variables of the $U3$ gate correspond to the θ and ϕ variables of the $|q\rangle^{\dot{a}}$ spinor. The decompositions for the helicity spinors are outlined in detail in Appendix B.2. To construct the scalar products $\langle pq\rangle$ and $[pq]$ on a quantum computer, unitary gates, $U_{\langle p}$ and $U_{[p}$, were created such that when they act on the $|q\rangle^{\dot{a}}$ and $|q]_a$ spinors, respectively, the scalar product values are associated with the complex coefficient of the $|0\rangle$ state. i.e. projecting out the $|0\rangle$ state or the probability of obtaining $|0\rangle$ is the associated scalar product amplitude squared. These gates and how to construct them using the basic 2 D QC gates are shown in Appendix B.2. It should be noted that the factors of $2E$ in the definition of the helicity spinors have not been accounted for, such that the spinor-qubit states are normalised to one on the quantum register. As a consequence, these factors must be added after the results have been obtained from the quantum computer.

4.3.2 1 → 2 amplitude calculation

A simple application of the helicity amplitude approach is the calculation of a 1 → 2 process. Here we will consider the process of $q \to gq$ by calculating the $gq\bar{q}$ vertex, where p_f and $p_{\bar{f}}$ are the momenta associated with the fermion and antifermion respectively. The gluon polarization vectors are defined as [92]

$$\epsilon_+^\mu = -\frac{\langle q|\bar{\sigma}^\mu|p]}{\sqrt{2}\langle qp\rangle}, \qquad \epsilon_-^\mu = -\frac{\langle p|\bar{\sigma}^\mu|q]}{\sqrt{2}[qp]}. \tag{4.3.5}$$

From expression it may be tempting to consider evaluating the four-vectors individually utilising the Pauli X, Y, and Z gates available as basic set of gates of any GQC, however, defining individual registers to evaluate independent components is unnecessary when overall results are Lorentz invariant and formed from Lorentz invariant scalar products. Therefore, using the Fierz identity [92]

$$\langle p|\bar{\sigma}^\mu|q]\langle k|\bar{\sigma}_\mu|l] = 2\langle pk\rangle[ql], \tag{4.3.6}$$

the amplitudes can be simplified as

$$\mathcal{M}_+ = -\sqrt{2}\frac{\langle p_f q\rangle [p_{\bar{f}} p]}{\langle qp\rangle}, \qquad \mathcal{M}_- = -\sqrt{2}\frac{\langle p_f p\rangle [p_{\bar{f}} q]}{[qp]}. \tag{4.3.7}$$

In this case only three qubits would be required to evaluate each scalar product involved in the amplitude respectively. The circuit for calculating this amplitude is shown in Fig. 4.2.

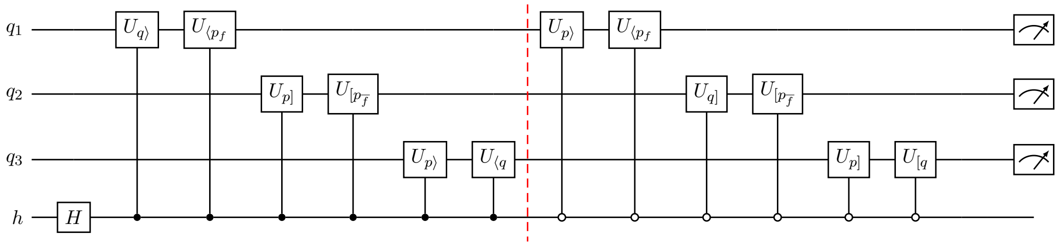

Figure 4.2: Detailed circuit diagram for the $q \to gq$ helicity amplitude calculation (taken from Reference [4]). The amplitude for the process is calculated on the q_i qubits, which are controlled from the helicity register. The q_i qubits are then measured by the quantum computer.

The unique quantum advantage is introduced by introducing a helicity register, where the rotation gates outlined in Appendix B.2 to form the scalar products can be controlled from the helicity register to form either amplitude $\mathcal{M}_\pm$ depending on the state of the helicity, where a $|0\rangle$ state on a single-qubit helicity register corresponds to a negative helicity and $|1\rangle$ to positive. This introduces direct entanglement between the helicity qubit, h, and the calculation qubits, q_i. Hence, by applying a Hadamard operation to the helicity register, a superposition of both helicity calculations is introduced to the q_i qubits. The three calculation qubits, q_i, are then measured by the quantum machine. How this algorithm scales for processes involving a large number of final state particles is discussed in detail in Sec. 4.3.4.

Fig. 4.3 shows the results of the algorithm for a random selection of small scattering angles, with runs on the IBM Q 32-qubit quantum simulator, called the `ibmq_qasm_simulator` [2], and the IBM Q 5-qubit Santiago Quantum Computer [93]; both of which have been compared to theoretical predictions of the probability distributions extrapolated directly from analytic calculations of the helicity amplitude, calculated using the S@M software [94]. The simulator has been run without a noise profile for 10,000 shots. The results from the quantum simulator show that the output of the quantum circuit lies within 1σ of the theoretically predicted probability distribution, where the errors were computed using the probability of each result and total number of shots. These were negligible and hence not shown within the figure of the results. From these distributions, one can determine the helicity setup of the process and consequently reconstruct the helicity amplitudes.

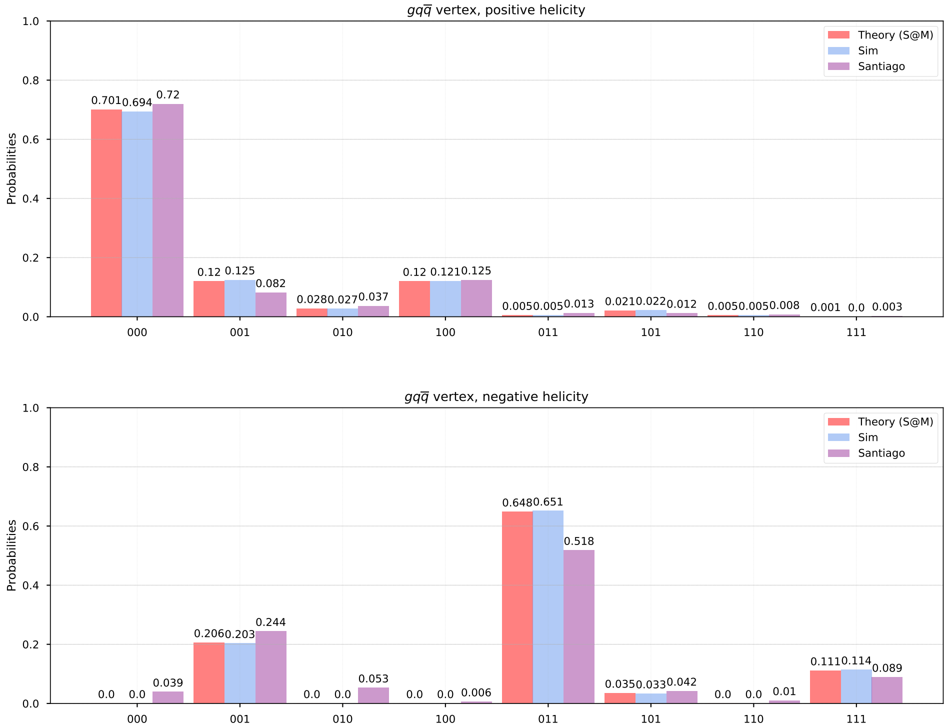

Figure 4.3: Results for the $q \to g\bar{q}$ helicity amplitude calculation (taken from Reference [4]). Comparison between theoretically calculated probability distribution, quantum simulator and real quantum computer.

The Santiago machine has been run on the maximum shot setting of 8192 for 100 runs, leading to a total of 819,200 shots of the algorithm. Fig. 4.3 shows the discrepancy between the simulator and the quantum computer which is expected for current quantum devices, as the fidelity of such quantum computers remains low, especially for algorithms with many multi-qubit operations. However, effective error mitigation schemes can be applied to the results.

The results from the quantum computer, shown in Fig. 4.3, have been achieved by isolating the individual helicity processes on the quantum circuit, by initialising the helicity register to specific helicity states $|0\rangle$ and $|1\rangle$ separately instead of using a superposition. The actual algorithm would contain a superposition of the helicity states through the implementation of a Hadamard gate on the helicity qubit. The helicity of the process is then determined by measuring the helicity register.

4.3.3 2 → 2 amplitude calculation

Extending from the 1 → 2 case in Sec. 4.3.2, the implementation of a full helicity amplitude calculation for the s- and t-channels of a 2 → 2 scattering process is outlined below. As an example, we consider a $q\bar{q} \to q\bar{q}$ process. The initial state quark and antiquark are labeled as particles 1 and 2 respectively and the final state quark and antiquark as 3 and 4. In total, there are only four nonzero helicity configurations possible for each s- and t-channel process. The relevant amplitudes are

$$\mathcal{M}_{s(+-+-)} = -\langle 2|\bar{\sigma}^{\mu}|1]\frac{1}{s_{12}}[3|\sigma_{\mu}|4\rangle, \quad \mathcal{M}_{s(+--+)} = -\langle 2|\bar{\sigma}^{\mu}|1]\frac{1}{s_{12}}\langle 3|\bar{\sigma}_{\mu}|4] \qquad (4.3.8)$$

where the +/ signs denote the helicity of the particles 1, 2, 3, and 4 and

$$\mathcal{M}_{t(++--)} = -\langle 3|\bar{\sigma}^{\mu}|1]\frac{1}{s_{13}}[2|\sigma_{\mu}|4\rangle, \quad \mathcal{M}_{t(+--+)} = -\langle 3|\bar{\sigma}^{\mu}|1]\frac{1}{s_{13}}\langle 2|\bar{\sigma}_{\mu}|4], \qquad (4.3.9)$$

the other nonzero amplitudes are obtained by complex conjugation. The calculation is performed in the center-of-mass (CM) frame and the momenta of individual particles are defined such that the only dependent input variable is the angle θ through which the quark (and antiquark) is scattered. In the CM frame, the overall magnitude of energy E associated with the momenta of each particle also drops out of the final helicity amplitude and is therefore not considered in this example. In the "all-outgoing" convention of spinor-helicity formalism [92], the momenta of incoming particles are flipped so that the incoming quark (1) (antiquark (2)) is mapped to an outgoing antiquark (quark) with opposite helicity. Again with application of the Fierz identity (Eq. (4.3.6)) and that $[p|\sigma^{\mu}|q\rangle = \langle q|\bar{\sigma}^{\mu}|p])$, the amplitudes in can be simplified to

$$\mathcal{M}_{s_{(+-+-)}} = 2\frac{\langle 24\rangle[31]}{\langle 12\rangle[21]}, \qquad \mathcal{M}_{s_{(+--+)}} = 2\frac{\langle 23\rangle[41]}{\langle 12\rangle[21]} \tag{4.3.10}$$

$$\mathcal{M}_{t_{(++--)}} = 2\frac{\langle 34\rangle[21]}{\langle 13\rangle[31]}, \qquad \mathcal{M}_{t_{(+--+)}} = 2\frac{\langle 32\rangle[41]}{\langle 13\rangle[31]}. \tag{4.3.11}$$

Using these expressions, the number of qubits needed for the circuit is four. On three of these qubits, each of the scalar products is calculated. The quark-antiquark vertex scalar products from the numerator are calculated on the first two qubits, and the denominator of the gluon propagator is calculated on the third qubit. Only one scalar product needs to be calculated for the denominator since the second scalar product can be determined via complex conjugation and therefore the scalar product is determined from the 0 probability of the third qubit. This simplified circuit is run on the `ibmq_qasm_simulator` [2] for 10,000 runs and compared to theoretically calculated probability distributions, extrapolated directly from analytic calculations of the helicity amplitude, calculated using the S@M software [94]. Using the equivalence between helicity spinors and orthogonal pure state qubits, these theoretical predictions have been obtained from the probabilities of each of the qubits to be in the $|0\rangle$ or $|1\rangle$ state, which correspond to the magnitude squared of the upper and lower components of the helicity spinor, respectively. The results from the quantum simulator show that the output of the quantum circuit lies within 1σ of the theoretically predicted probability distribution and are shown in Fig. 4.4 for both the *s*- and *t*-channel processes in a specific helicity configuration.

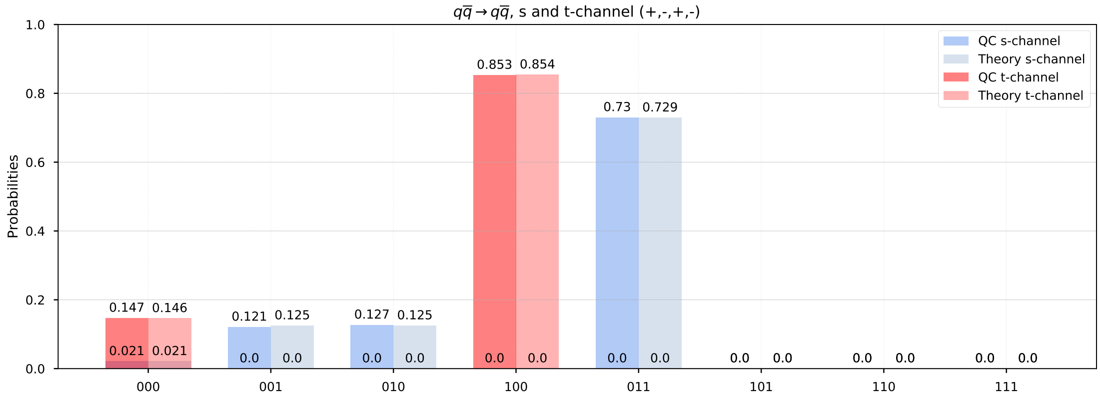

Figure 4.4: Comparison between theoretically predicted qubit final state probabilities and 32-qubit quantum simulator output for the s and t-channel $q\bar{q} \to q\bar{q}$ process in the (+,-,+,-) helicity configuration (taken from Reference [4]). The quark (antiquark) scattering angle has been chosen as $\theta_3 = \frac{\pi}{4}$. Negligible error bars have also not been displayed as before.

4.3.4 Generalization to 2 → n amplitude calculations

It is known that by studying the properties of the analytic structure of these tree level amplitudes of on-shell massless partons, recursive relations can be formed, such as the BCFW recursion relations of Britto, Cachazo, Feng, and Witten [95, 96], which have helped derive remarkably simple expressions for general n-point tree-level amplitudes for massless partons. For example, the infamous Parke-Taylor formula [97] which gives an expression for a general n-point gluon amplitude in Yang-Mills theory for a maximally helicity violating amplitude as

$$\mathcal{A}_n[1^+ \cdots i^- \cdots j^- \cdots n^+] = (-g_s)^{n-2} \frac{\langle ij \rangle^4}{\langle 12 \rangle \langle 23 \rangle \cdots \langle n1 \rangle}. \tag{4.3.12}$$

Generally, in the spinor helicity formalism, a tree amplitude of massless particles is a rational function of the (complex-valued) kinematic invariants $\langle ij \rangle$ and $[ij]$.

Consequently, the algorithm presented in Secs. 4.3.2 and 4.3.3 can be generalised to multi-particle amplitudes straightforwardly as the tools are already created, namely the circuit decompositions of the helicity spinors from Appendix B.2. Since E is an input to the calculation of the squared matrix element even for very large n, including the multiplicative factors of $2E$ for each particle remains straightforward. The number of calculation qubits, q_i, and the number of helicity qubits, h_i, needed in the algorithm both scale linearly with the number of final state particles, n. As the number of helicity qubits, h_i, scales linearly, then so does the number of work qubits needed in the algorithm. Each scalar product calculation requires two spinor operations, and so the algorithm can be easily extended without adding disproportionate complexity. The circuit depth scales linearly with an increase in the number of scalar products, calculated on the q_i qubits, and the number of helicity qubits, h_i, added to the circuit.

Currently, the algorithm is restricted to massless partons by exploiting the BCFW recursion formula. The advancement in quantum technologies will make the implementation of the full algorithm, capable of simulating massive partons, computationally feasible, thus extending the ability of the proposed helicity amplitude algorithms.

Chapter 5

Quantum Monte Carlo Parton Shower

In the previous chapter, we constructed a quantum algorithm for calculation of helicity amplitudes on a GQC by exploiting the equivalence between helicity spinors and qubits, demonstrating a unique quantum advantage as a result the natural formulation of quantum mechanical scattering amplitudes on a QC. In this chapter, we present the first implementation of a QCD parton shower algorithm on a quantum device, summarising the findings in Reference [4]. The algorithm constructs a collinear QCD model with one gluon and one (flavour of) quark. The theoretical framework of the simple QCD model is outlined in Sec. 5.1. The quantum implementation of a general and extendable parton shower algorithm is outlined in Sec. 5.2, with circuit sub-operations outlined in Secs. 5.3-5.7, and the results from the simulation of two shower steps on the `ibmq_qasm_simulator` [2] device are presented in Sec. 5.8 .

5.1 Collinear Parton Shower on a Quantum Device

The complexity of simulating parton showers is increasing rapidly with the use of classical methods such as MC event generators. Hence, we require new methods to improve the accuracy and efficiency of parton shower algorithms to capture the high multiplicity events of processes at higher energy and higher luminosity colliders. New methods proposed on the quantum computing paradigm could be used to enhance or speedup existing parton shower algorithms, capturing quantum interference effects currently not included in classical algorithms. In this section, we introduce the theoretical framework for a simple, collinear QCD model-parton shower based on the Monte Carlo approach from Sec. 2.4.2. We will see how such a model could be implemented on quantum computing framework with a general quantum algorithm outlined for qubit-based quantum machine described in Sec. 5.2. The algorithm has been designed to run on the 32-qubit `ibmq_qasm_simulator` and under this qubit number constraint we consider a simplified QCD toy model consisting of one gluon and one quark flavour only. Also, restricting ourselves to a model of massless particles and collinear splittings only, the DGLAP splitting kernels from Eqs. (2.4.2) and (2.4.3), taking $n_f = 1$ and $N_c = 3$ are

$$P_{gq}(z) = \frac{4}{3}\Big[\frac{1+(1-z)^2}{z}\Big], \tag{5.1.1}$$

$$P_{gg}(z) = 3\Big[2\frac{1-z}{z} + z(1-z)\Big], \tag{5.1.2}$$

$$P_{q\bar{q}}(z) = \frac{1}{2}\Big[z^2 + (1-z)^2\Big], \tag{5.1.3}$$

where z is the fraction of parton i's momentum carried by parton j in the splitting $i \to jk$. Unlike in the classical algorithm, the evolution variable which we take as z, is discretised where each interval denotes a single step in the shower. As a further simplification, we discretise the shower into individual shower steps and only evolve the variable z, removing the need to keep track of individual particle kinematics. We can therefore write the Sudakov factor from Eq. (2.4.6) for a given step between the evolution variables z_1 and z_2 (where $z_2 < z_1$), as the parton evolves down to smaller energy scales, in the form

$$\Delta_j(z_1, z_2) = \exp\left[-\alpha_s^2 \int_{z_1}^{z_2} P_{ji}(z) dz \right] \tag{5.1.4}$$

so that the total non-emission probability at step N is defined as

$$\Delta_{\text{tot}}(z_1, z_2) = \Delta_g^{n_g}(z_1, z_2) \Delta_q^{n_q}(z_1, z_2) \Delta_{\bar{q}}^{n_{\bar{q}}}(z_1, z_2), \tag{5.1.5}$$

where n_g,n_q and $n_{\bar{q}}$ are the number of gluons, quarks, and antiquarks respectively that are present at step N. The parton shower allows for only one emission per shower step, so that $\left(n_g + n_q + n_{\bar{q}}\right) \leq N$. With limited qubits we also consider the simplified case and neglect running of the strong coupling and set $\alpha_s = 1$, where $\alpha_s = \frac{g_s^2}{4\pi}$.

5.2 Quantum Circuit Implementation

The quantum circuit for the quantum parton shower algorithm comprises of 4 registers: the *parton* register, *counting* register, *emission* register and *history* register. The algorithm is executed for incremental shower steps in terms of the discretised evolution variable, z, where individual step involves 4 operations: the *counting* operation, *emission* operation, *history* operation, and *update* operation. The steps are the iterated by updating the evolution variable evolving the parton shower algorithm in z towards lower momentum scales. Each of the operations is derived from the decomposition of a multi-controlled rotation as shown in Fig. 5.1, which requires $(n-1)$ ancillary qubits for an n-controlled rotation.

A final measurement is performed after the total number of iterations required for

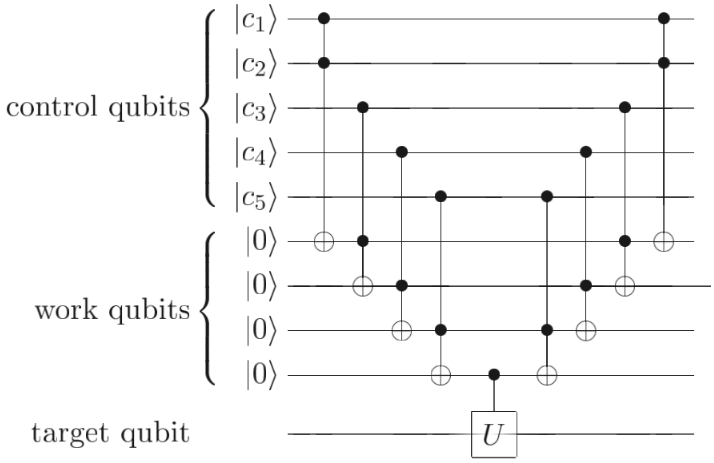

Figure 5.1: Circuit diagram for multi-controlled rotation decomposition, taken from [1].

evolution up until the cutoff in z, as done for the Monte Carlo approach, and the final state is projected onto a register of classical bits. The algorithm is repeated to obtain the probability distribution of all the possible final state configurations and hence parton shower histories. A schematic of the quantum parton shower circuit is shown in Fig. 5.2.

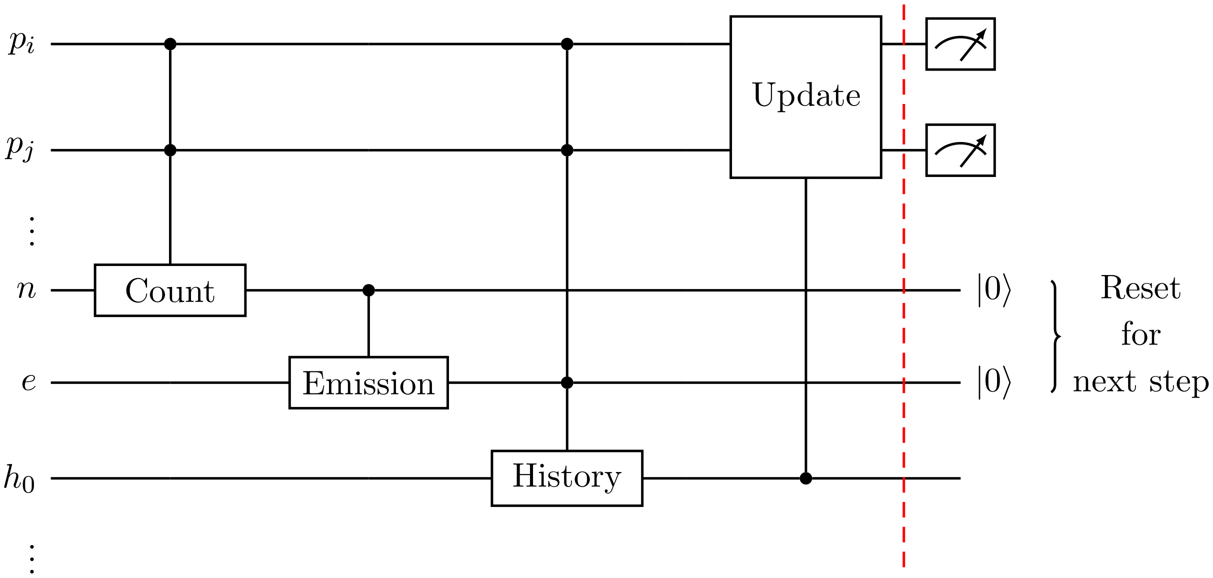

Figure 5.2: Circuit diagram for one step of the algorithm (taken from Reference [4]). The circuit comprises of particle registers, emission registers and history registers.

Below, we introduce the individual operation sub-circuits and outline their roles in the circuit. The first step of the parton shower is setting up the initial parton: either a gluon or a (anti)quark, which is carried out by initialising the parton register. The partons are encoded in a three-qubit state where $|100\rangle$, $|001\rangle$ and $|011\rangle$ correspond to a gluon, quark and antiquark respectively. Hence, the initial parton is set up by applying NOT gates to the qubits corresponding to "1". A null state is also introduced, defined as $|000\rangle$ in the binary basis, to denote the absence of a parton. The first initial parton three-qubit state is labelled as p_0 and subsequent partons added in the shower are added in separate registers $p_i, i = 1, ..N$, where N is the number of steps and also the maximum number of additional partons given only a single possible emission per step. The total number of binary states for three qubits is eight, so the model can easily be extended to include more flavours i.e. seven parton species (excluding null state).

5.3 Counting Operation

The first operation in the algorithm is the counting operation, C_f, which determines the number of each type of parton at the start of each step in the shower. This is done by control operations from the parton registers, p_i, to determine each parton state and increase the occupation number of the associated count registers, labelled n_g,n_q and $n_{\bar{q}}$ for the gluon, quark and antiquark count registers respectively. Fig. 5.3 shows a schematic of the count operation applied to a parton sub-register p_k. In this example, it is constructed from a counting mechanism to detect the gluon parton type and a subsequent update to the appropriate count register. These count operations are extended to the other parton types and are applied to each parton sub-register p_i. The number of qubits required for each register is the number of qubits required to represent the number of partons at a given step and hence scales as

$$n_{\text{qubits}}^{\text{count}} = 3\left[\log_2\left(\mathrm{N}+1\right)\right] \tag{5.3.1}$$

i.e. logarithmically with number of steps. For a two-step parton shower, the counting register requires four qubits: two for the gluon count sub-register, and one for each quark and antiquark sub-register. This is understood by seeing that only a single quark/antiquark exists after the first step whilst two gluons are possible.

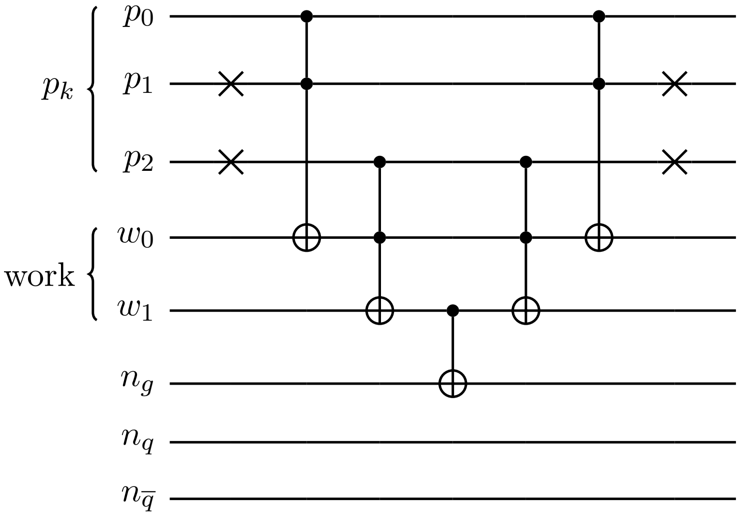

Figure 5.3: Count gate circuit decomposition for counting a gluon in the particle register (taken from Reference [4]). To complete the count gate, this is repeated for all other possible particle types by applying different combinations of *NOT* gates.

The count operation is constructed from a series of multi-controlled gate operations: CCNOT and CNOT gates where a total of 15 gates is necessary to each particle sub-register at each step. For a total of N steps, with $N+1$ possible partons at a given step, the number of gate operations required to implement the count operation scales as

$$n_{\text{gates}}^{\text{count}} = 15\frac{N\,(N+1)}{2}. \tag{5.3.2}$$

5.4 Emission Operation

As in the Monte Carlo approach from Sec. 2.4.2, the next step is determining whether an emission occurs in a momentum interval z_1 to z_2 using the Sudakov factors. This is implemented in the quantum circuit by encoding the emission $(1-\Delta_{tot})$ and non-emission (Δ_{tot}) probabilities in a single qubit rotation as

$$E_f = \begin{pmatrix} \sqrt{\Delta_{\text{tot}}\left(z_1, z_2\right)} & -\sqrt{1-\Delta_{\text{tot}}\left(z_1, z_2\right)} \\ \sqrt{1-\Delta_{\text{tot}}\left(z_1, z_2\right)} & \sqrt{\Delta_{\text{tot}}\left(z_1, z_2\right)} \end{pmatrix}, \tag{5.4.1}$$

which rotates between the single-qubit basis states $|0\rangle$ and $|1\rangle$ which correspond to an emission and non-emission respectively. Hence a non-zero Sudakov factor and hence emission probability when applied to a single-quit emission register, e_i, will form a superposition of emission and non-emission histories (this coherence is maintained for each step until the final measurement). Quantum coherence is evident by considering the parton register initialised in a superposition of the three possible states: gluon, quark and antiquark, where controlling from the register (and count register) once emission operation is applied to the register, the state will be in a superposition of all possible emission histories associated with all three particles. As the shower steps continues to iterate, the emission operation must control from the updated count registers for all partons, accounting for all possible emissions from existing partons. Given that only a single emission can occur for each step, a choice must made for the parton which is responsible for emission. This is dealt with in the update operation, which is done by recording the emission probabilities for each parton. For N shower steps, with N maximum possible emissions, the emission register scales as

$$n_{\text{qubits}}^{\text{emission}} = N \tag{5.4.2}$$

such that the emission probabilities of the parton in sub-register p_i are encoded onto the emission register qubit e_i.

Since the emission operation controls from the count registers, similarly to the count operation, there must be a multi-controlled operator which consistent of several of CCNOT gates and a controlled rotation. This is shown in an example shower content with a single gluon in Fig. 5.4. Again, the number of CCNOT gates required to decompose a multi-controlled rotation is $2(n-1)$, where n is the number of controls. Therefore, the number of gates required to implement the emission operation is

$$n_{\text{gates}}^{\text{emission}} = 12\left(3\left\lceil \log_2(N+1)\right\rceil - 1\right) + 6N. \tag{5.4.3}$$

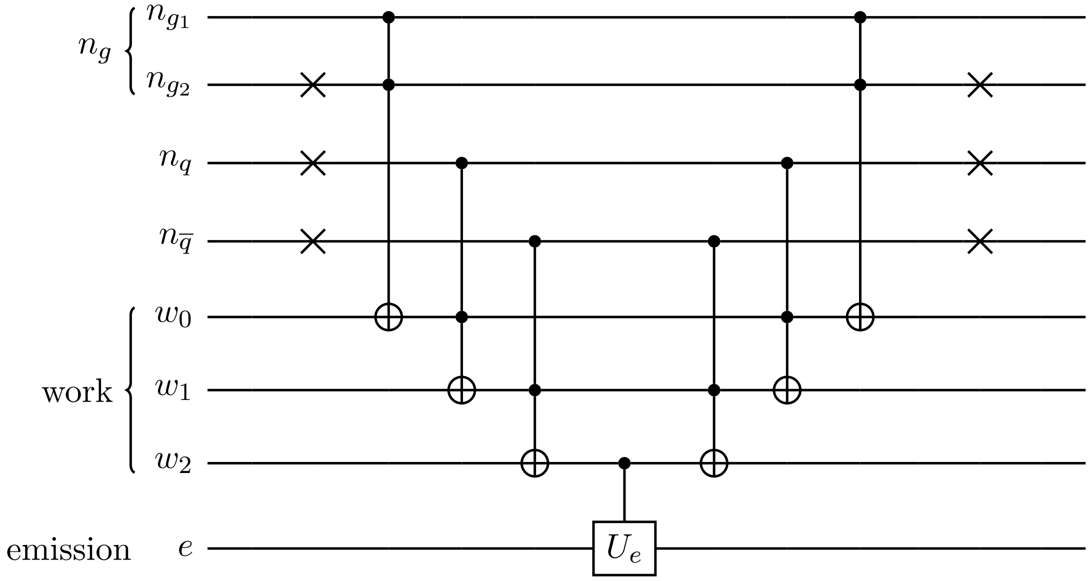

Figure 5.4: Emission gate for a single gluon in the first particle register (taken from Reference [4]). Here U_e is a U_3 rotation used to implement the Sudakov factors.

5.5 History Operation

Determining which parton emits at a given step as well what the type of splitting and hence what the resulting partons are in the subsequent step is determined by the History operation. This operation encodes all splitting probabilities onto the circuit via the history rotation

$$H_f = \begin{pmatrix} \sqrt{1-\hat{P}(z)} & -\sqrt{\hat{P}(z)} \\ \sqrt{\hat{P}(z)} & \sqrt{1-\hat{P}(z)} \end{pmatrix}, \tag{5.5.1}$$

where $\hat{P}(z) = \left(P_{ji}(z)/P_{\text{tot}}(z)\right)$ and

$$P_{\text{tot}}(z) = n_g\left(P_{qg} + P_{gg}\right) + n_q P_{gq} + n_{\bar{q}} P_{gq}. \tag{5.5.2}$$

One aspect of the history operation to highlight are the two possible gluon splittings in comparison to the single type of quark splitting. The approach to handling the extra complexity introduced by the gluon splittings is outlined below in the description of the history implementation. The history register is partitioned into three sub-registers according to the three types of splitting possibilities: the gluon histories, quark histories, and antiquark histories (where the gluon history sub-register requires twice the amount of qubits as the (anti)quark sub-register). The history register scales with respect to the number of steps N as

$$n_{\text{qubits}}^{\text{history}} = 4\frac{N\,(N+1)}{2}. \tag{5.5.3}$$

The schematic of the history operation is shown for a single gluon in the first step in Fig. 5.5 which displays how the operation controls from both parton registers, p_k, as well as emission register, e, (i.e. only apply probability of splitting to history register if there was an emission and if the initial parton associated with said splitting is seen in register) and applies the H_f rotation from Eqs. (5.5.1) to the history sub-registers, h_i, encoding the splitting information onto the history registers. We can effectively reduce qubits and gate count of the algorithm by exploiting $q\bar{q}$ symmetry in the splitting functions, thus requiring only one history sub-register for the quark and antiquark species.

The history operation is also constructed from a series of CCNOT gates and a controlled-rotation, where the number of gates required to implement the history gate at step N is given by

$$n_{\text{gates}}^{\text{history}} = 16\frac{N\,(N+1)}{2}. \tag{5.5.4}$$

The quadratic scaling of the number of gate and qubits for the history operation means it is the costliest operation in the quantum parton shower algorithm. This scaling means an actual implementation with large coherence times and small environmental errors on the NISQ devices is impractical and so the algorithm is instead implemented on the `ibmq_qasm_simulator` [2] device, which can simulate

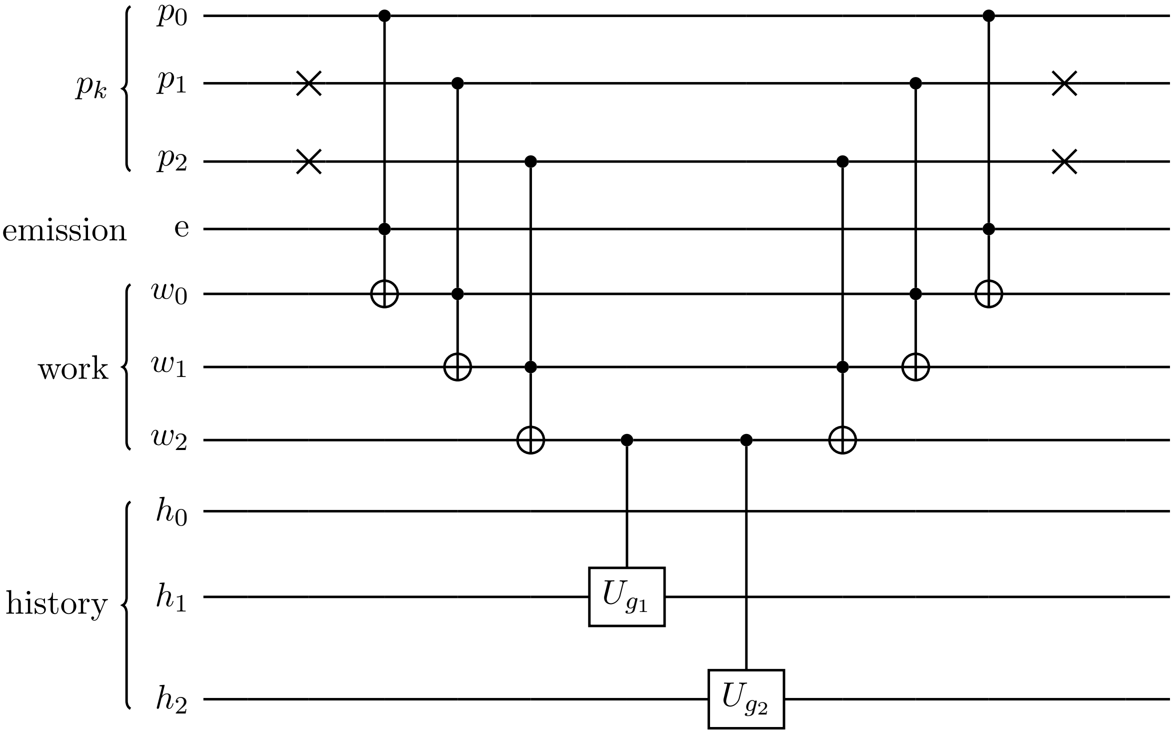

Figure 5.5: History gate for a single gluon in the first step (taken from Reference [4]). Here the U_{g_i} gate is a U_3 rotation used to implement the splitting probabilities.

a fault-tolerant device, as proof-of–principle. This could then in principle be actually implemented after the eventual realisation of fault tolerant computation in the future.

5.6 Resetting the Emission and Counting Registers

A small comment to be made, is the use of resetting on both the emission and counting registers at the end of each step. This is possible since the history register, controlling from the emission registers (and hence counting registers and the parton registers), encodes all the information needed to propagate the shower to the next step by inheriting the Sudakov factor information from the emission operation and splitting probabilities. This reset is achieved by inverting the unitary operations in both emission and counting operations prior to beginning the update operation. Resetting is only referred to here in the quantum sense via unitary operation, not classically via irreversible decoherence or measurement, hence all parton shower histories remain coherent in superposition. Resetting is also a crucial tool for resource-efficiency in the algorithm as it means additional qubits are not required, improving the scaling of qubits.

5.7 Update Operation

The final operation in a shower step is to update the particle content of the shower depending on splitting probabilities encoded on the history registers. The schematic for the first step is shown in Fig. 5.6 and is applied iteratively over the parton sub-registers, p_i. It consists of three controlled operations, controlling from the three types of splittings encoded in the history sub-registers, and then updating the parton content of existing registers as well as populating a new one for a given emission. The first controlled operation populates the p_j sub-register with a gluon, simulating the emission of a gluon from a (anti)quark from the original p_i parton register. The second controlled operation updates according to the splitting of a gluon to a quark-antiquark pair controlling from the h_1 register. This first removes the existing gluon to create a null state in the p_i register, then populates the p_i and p_j with a quark-antiquark pair. Given the two possibilities in the quark-antiquark ordering in the p_i and p_j registers, a controlled-Hadamard gate and subsequent CCNOT gate is used to create an equal superposition of quark-antiquark pairs on the pair of registers. An initial NOT gate is applied to the third qubit of the p_i and p_j registers, common to both q and $\bar{q}$, then a Hadamard is applied to the middle qubit of the p_j register where a further controlled operation from the $|0\rangle$ state in the middle qubit is used to apply a NOT on the first qubit of the p_i register. Hence, for a $|0\rangle$ state on the middle qubit for p_j (i.e. a quark on p_j) leads to a flip on the p_i middle qubit and therefore an antiquark on the p_i register, otherwise a $|1\rangle$ state (i.e. antiquark in the p_j register) leaves the quark state on the p_i register. The final controlled operation is for the update associated with the $g \to gg$ splitting, which simply populates the p_j register with a gluon given the p_i with a gluon. However, a distinct feature to this model is the preferential treatment of the splitting $g \to q\bar{q}$ over $g \to gg$. This is encoded onto the device by using a $|0\rangle$-control on the h_1 qubit when populating p_j.

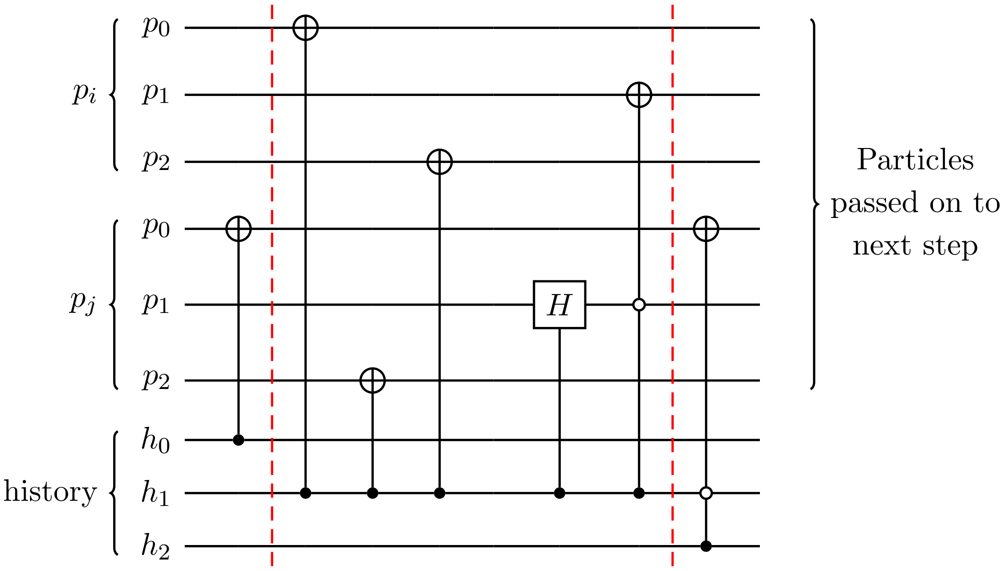

Figure 5.6: Update gate for the first step of the algorithm (taken from Reference [4]). Each slice is a different update mechanism: far left slice updates $q \to qg$ splittings, centre slice updates $g \to q\bar{q}$ and the far right slice updates $g \to gg$.

However, since there can only be one emission for a given step, for multiple possible emissions from the partons a choice on the parton to emit has to be made. This done by the "oldest" partons in the shower to emit first so that the update operation will allow for parton i to emit over parton j if $i < j$. The number of operations to implement the update operation is

$$n_{\text{gates}}^{\text{update}} = 7\frac{N\,(N+1)}{2}. \tag{5.7.1}$$

Like the history operation, there is quadratic scaling in the number of required gates. However, the update gate is constructed mainly from single controlled gates, which are not as computationally expensive as multi-controlled gates, such as the CCNOT and so is not as costly as the counting and history operations, which grow quadratically in the number of required CCNOT gates. After the update operation is complete, the entire step with all sub-operations is repeated for the desired number of steps, constructing a highly entangled final state that holds the information of all possible shower histories. Measurement of the parton register then projects out a single final state configuration. The shower is then repeated to build a probability distribution for the shower process.

5.8 Results

The collinear QCD quantum parton shower has been run for two shower steps on the `ibmq_qasm_simulator` [2] device for both an initial gluon and quark. The algorithm has been run with 10,000 shots with each shower step run with a fixed interval, $0.3 \leq z \leq 0.5$, for simplicity. The simulator device was run without a noise profile to replicate the results of a fully fault tolerant device. These results are displayed in Fig. 5.7 where the antiquark parton distribution has been omitted, due to its equivalence to the quark distribution as seen from the symmetry of the (anti)quark splitting kernel.

The results are in agreement to within 1σ of the theoretically calculated probabilities which were computed analytically using the collinear splitting functions and Sudakov factors. The negligible 1σ error bars from the quantum simulator output, as calculated previously using individual probabilities of outputs and total number of shots, have also been omitted from the diagram.

For both distributions in Fig. 5.7, there is an excess in the shower histories that involve a $g \to q\bar{q}$ splitting, which is attributed to the preference given to this splitting over $g \to gg$ in the update operation.

A general and extendable collinear QCD parton shower has been implemented on a quantum device for a single flavor of quark and gluon. Inspired by the classical Monte

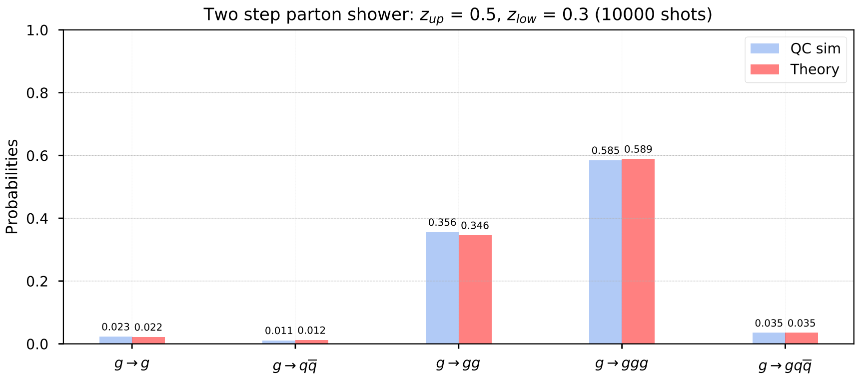

(a) Initial particle a gluon.

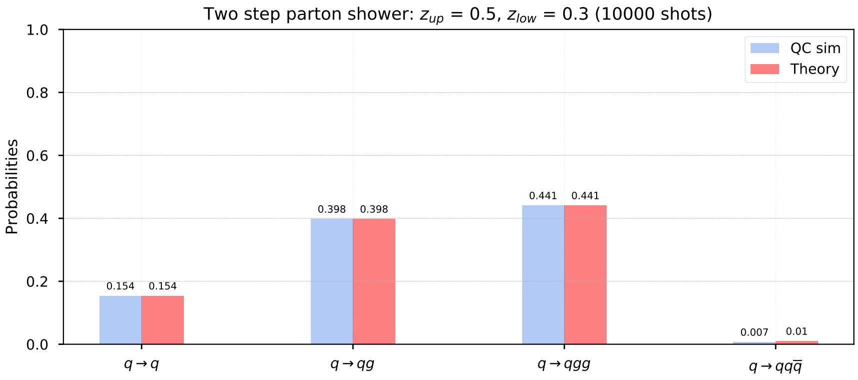

(b) Initial particle a quark.

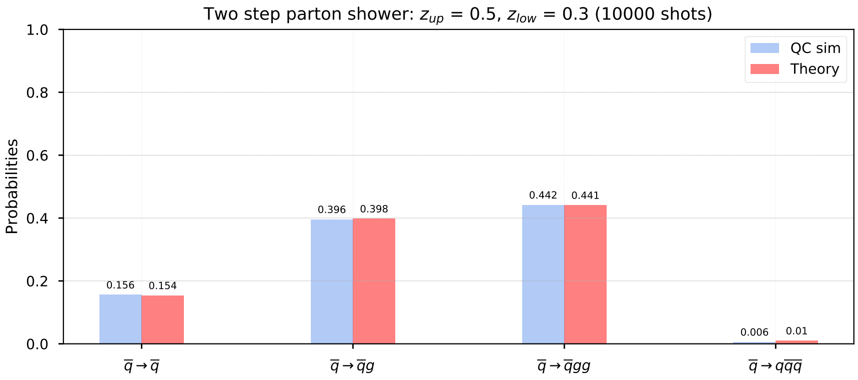

(c) Initial particle an antiquark.

Figure 5.7: Results from the quantum circuit compared to theoretical predictions for two steps of the parton shower with momentum interval of $z_{\text{lower}} = 0.3$ to $z_{\text{upper}} = 0.5$ and the initial state particle of (a) gluon, (b) quark and (c) antiquark (taken from Reference [4]).

Carlo algorithm the parton shower is built on the same principles of radiation dominated by collinear divergences, but unlike the classical algorithm, it includes quantum interference effects between all possible shower histories maintained throughout the evolution of the parton shower. This leads to a distinct and unique advantage possibly providing useful insight to simulation of scattering process at colliders in the future. The algorithm has been run on the 32-qubit `ibmq_qasm_simulator` to simulate two shower steps and is constructed from 31 qubits and 444 gate operations (including 169 single qubit gates, 217 CCNOT gates and 58 CNOT gates). The scaling of the algorithm has been shown to be quadratic in the number of qubits and the number of gates required. Although not implementable on NISQ devices in current use, with future potential of fault tolerant computation, the parton shower can be easily implemented from the existing proposal and extended to multiple quark flavours and parton species for a more accurate QCD parton shower simulation.

Chapter 6

Quantum Walk Approach to Parton Showers

The implementation of the quantum parton shower algorithm in chapter 5 is based on the principles of the classical Monte Carlo approach and is a first demonstration of a proof-of-principle toy QCD model parton shower on a GQC. However despite this, the computational costs from the quadratic scaling of the algorithm of qubits and circuit depth means a practical implementation on NISQ era-device, with limited number of qubits and decoherence times, remain unfeasible. The demonstration on the 32-qubit `ibmq_qasm_simulator` [2] also proved to be costly with significant simulation times, leading to only a maximum two-step implementation. Despite the unique advantages introduced by the quantum algorithm, this fails to compare to the current-state of art classical implementations via Monte Carlo algorithms.

In order to match realistic shower depths of classical simulations, methods to minimise qubit and gate requirements for each step must be realised. In this chapter we present a novel approach to a quantum simulation of a parton shower which utilises the quantum walk algorithm (described in Sec. 3.2), creating a natural compact framework for a quantum parton shower simulation in comparison to previously developed quantum algorithms, summarising the findings in Reference [3]. In Sec. 6.1 we extend the theoretical foundation of the quantum parton shower towards the quantum walk framework where in Sec. 6.2 we begin by introducing a simple example for a scalar theory with single splitting to demonstrate the principles of the algorithm on a discretised 1 D line. This then leads to a simulation of a collinear QCD parton shower in Sec. 6.3. The merits of a paradigmatic shift from classical to a truly quantum framework within the quantum walk algorithm is discussed in Sec. 6.4, and shown to provide significant improvements towards simulating a full, realistic QCD parton shower with efficient quantum resource scaling.

6.1 The Parton Shower as a Quantum Walk

Under the same theoretical framework as Sec. 5.1 the shower is discretised into steps defined by discrete values of the evolution variable, z, with only one possible emission per step. The overall probability for emission at a step defined in terms of the Sudakov factor, Δ, in equation Eq. (5.1.5), and the splitting kernel, P, defined in Eq. (5.5.2), is given by

$$\hat{P}'_{ji} = (1 - \Delta_{\text{tot}}) \times P_{tot}. \tag{6.1.1}$$

This probability will be seen to be encoded into the quantum coin operation that was defined in the discrete QW formalism (Sec. 3.2). In the QW framework, a significantly large number of steps can be simulated in comparison to previous quantum algorithms. The shower is evolved downwards in momenta, i.e. towards exponentially lower z values with the number of steps. In these simulations a purely arbitrary step cutoff is chosen but can be set by the physical scales of the process for future implementations.

6.2 Scalar Quantum Walk Shower

Using the framework outlined in section Sec. 3.2 the quantum walk is constructed from the tensor product of two Hilbert spaces: the position space $\mathcal{H}_P$ and the coin space $\mathcal{H}_C$. This Hilbert space can also be augmented by an additional one denoted, $\mathcal{H}_M$, for the memory of the walker of the previous occupied positions which is used for implementations of a quantum walk with memory, but we will not consider this here and more information on the subject can be found in [5,98,99]. Each individual step of the quantum walk consist of a coin operation in $\mathcal{H}_C$ which instructs the movement of the walker and a subsequent shift operation controlled from the coin register to carry out the corresponding shift in position space $\mathcal{H}_P$.

As a simple demonstration for proof of concept, a simple scalar theory is considered which will be used to introduce all three components of the circuit design required to implement a quantum walk parton shower algorithm.

In the scalar theory, we consider only a single scalar particle, ϕ, with splitting channel $\phi \to \phi\phi$ according to the probability

$$\hat{P}'_{\phi\phi} = \Big(1 - \Delta_\phi\Big) \times P_{\phi\phi}. \tag{6.2.1}$$

The rotation encoding this splitting probability is given by

$$C_{\phi\phi} = \begin{pmatrix} \sqrt{1 - \hat{P}'_{\phi\phi}} & -\sqrt{\hat{P}'_{\phi\phi}} \\ \sqrt{\hat{P}'_{\phi\phi}} & \sqrt{1 - \hat{P}'_{\phi\phi}} \end{pmatrix}, \tag{6.2.2}$$

which is used as the coin operation for the quantum walk such that the basis states of the coin space, $|0\rangle$ and $|1\rangle$, correspond to non-emission, $\Big(1 - \hat{P}'_{\phi\phi}\Big)$, and emission, $\hat{P}'_{\phi\phi}$, probabilities respectively.

Given that the splitting can only increase the number of ϕ particles by one at a given step (or remain the same for non-emission), we can represent the position space states to encode the number of ϕ particles where emissions correspond to movement along the $+x$ direction along the ϕ axis. Summarising this, the position space $\mathcal{H}_P$ is to span only zero and positive integers, $\{|i\rangle :\in \mathbb{N}_0\}$, where $|i\rangle$ represents i particles in the computational basis. Using the coin operation in combination with the position space, a 1 D quantum walk scalar shower is defined and shown schematically in Fig. 6.1.

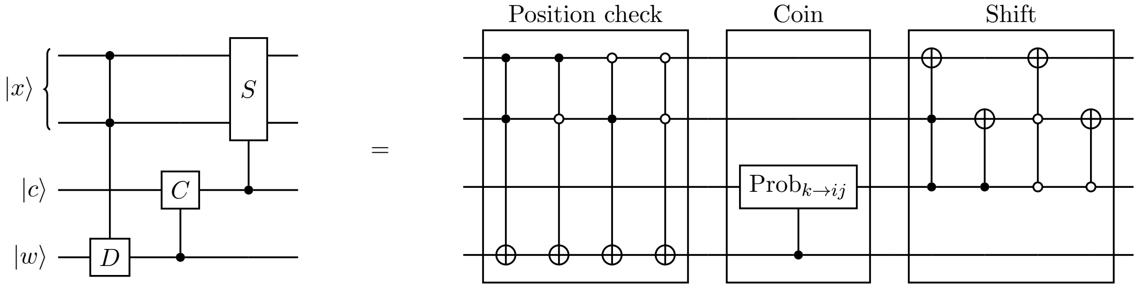

Figure 6.1: Template for a single step of a quantum walk as a parton shower for a simple scalar theory model, with the ability to simulate a single scalar particle with single splitting (taken from Reference [3]). The "*position check*" determines the number of particles present by assessing the position of the walker. The "*coin*" operation applies the correct splitting probabilities depending on the position of the walker. The "*shift*" operation moves the walker depending on the outcome of the coin operation.

Here the circuit is shown to be constructed from three registers: the position register, x, which encodes the number of particles in the shower using the computational basis, the coin register, c, and the work register, w, used to implement the position dependent coin operation. The number of particles that can be simulated by the quantum walk shower scales exponentially with the number of qubits in the position register, n_x, such that

$$\text{Maximum number of particles} = 2^{n_x} - 1. \tag{6.2.3}$$

6.2.1 Coin Operation

The first operation at a given step is the coin operation, where the coin register is initially set up in the default $|0\rangle$ non-emission qubit state. After application of the coin rotation (6.2.2) the coin register, c, is in a superposition of the states $|0\rangle$ and $|1\rangle$ with probabilities corresponding to non-emission and emission respectively. Given that the coin operation includes the Sudakov factor and the splitting kernels, it must depend on the shower content and shower evolution variable (z) at each step, i.e. the number of particles must be determined at each step, which is defined by a "position check" operation. The position check operation controls from the position space register to determine which number basis the register is in, and subsequently updates an ancillary qubit. The ancillary qubit is then used as a control to act on the coin register, c, with the correct splitting probability, $\hat{P}'$. After applying the coin operation, the ancillary qubit can be returned to the ground state $|0\rangle$ by performing the (unitary) inverse of the position check operation so that the same ancillary qubit can be used for each position check. The coin and the position check operations are then applied for each combination of intermediate shower states. The number of qubits required for the coin register, c, is equal to the number of splitting kernels (which in this simple scalar case is one) whilst the number of qubits required for the ancillary register, a, is equal to the number of species in the shower. The number of the single scalar particles for the shower is encoded in the position register, x, where the number of required qubits grows logarithmically with the maximum number of shower steps for the register. Therefore, the number of gates needed for the position check and coin operations after N steps is

$$n_{\text{gates}}^{\text{coin}} = N \left(2 \left\lceil \log_2 \left(N_{\max} + 1\right) \right\rceil - 1\right), \tag{6.2.4}$$

where $N_{\max}$ is the maximum number of steps in the shower corresponding to the maximum number of particles which could be emitted over the shower process.

6.2.2 Shift Operation

The next stage of the step is the shift operation where the dynamics of the walker is determined from the coin space which at this point in a superposition of emission or non-emission states according to the splitting probabilities due to the coin rotation in Eq. (6.2.2). The shift operation either increments the position of the walker when the coin register is in $|1\rangle$ state, or leave the position unchanged corresponding to no emission when the coin register is in the $|0\rangle$ state. A schematic for the shift operation for the scalar shower is shown in Fig. 6.2, which shows the increment operation controlled from the coin register, that is formed from a series of multi-

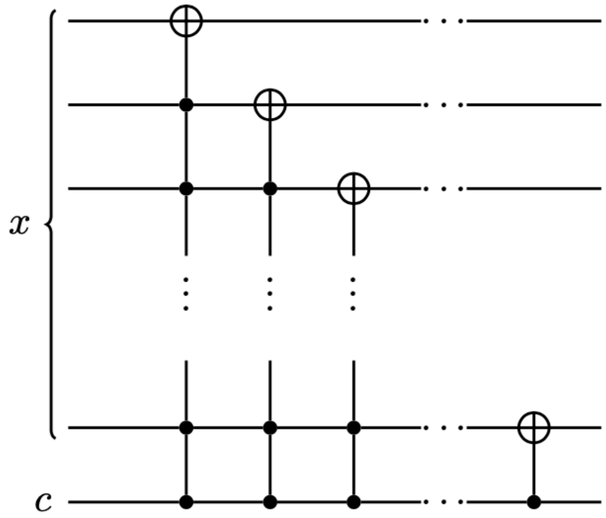

Figure 6.2: Schematic for the shift operation for the scalar QW which shows the increment operation to the position register is controlled from the coin register.

controlled NOT gates.

Similarly, a decrement operator can be defined which reduces the position space state by one which can be constructed in the same way but by controlling from a $|0\rangle$ state instead (or through an alternative method discussed in [100]). This will be needed for the full toy QCD collinear shower in Sec. 6.3, which will be used to decrease the number of partons for the additional types of splitting channels.

The number of gates required to implement the shift operation is identical for each step and is equal to $\left(\lceil\log_2\left(N_{\max}\right)\rceil\right)^2$, which is the number of gates to increment the position of the walker (equivalent to the number of qubits in the position register squared). The circuit depth of the shift operation for the N-step shower grows linearly with N as,

$$n_{\text{gates}}^{\text{shift}} = N\left(\lceil\log_2\left(N_{\max}\right)\rceil\right)^2 \tag{6.2.5}$$

where $N_{\max}$ is the maximum number of steps in the shower, which corresponds to the maximum number of particles that can be simulated.

6.3 Quantum Walk Parton Shower

Following on from the scalar shower outlined in Sec. 6.2, it is possible to build a quantum walk that can simulate the discrete, collinear QCD model from chapter 5. As in the simplified collinear model for MC-inspired quantum parton shower algorithm, a single gluon and quark flavour is considered with three possible splitting channels shown in Eqs. (5.1.1) to (5.1.3). Given now that there are two types of partons, the QW from the scalar model is extended to a 2 D case, where the number of each parton type is given by the (x, y) axis respectively for the quantum walker where the position space, $\mathcal{H}_P$, now spans $\{|i\rangle, |j\rangle; i, j \in \mathbb{N}_0\}$. Here, due to the symmetry of the $q\bar{q}$ states from the splittings, only a single dimension is required to represent the total number of quark-antiquark pairs. As well as increasing the dimension of the position space, the coin space must also be expanded to include the additional splittings. The single scalar splitting was encoded into the single qubit coin basis states, $|0\rangle$ and $|1\rangle$, whilst the QCD model will require three coins for the three types of splittings.

6.3.1 Coin Operation

For the QCD parton shower, there are three splitting kernels which are encoded onto three coin qubits using controlled rotations of the form shown in Eq. (6.2.2). Similarly to the quantum walk for the scalar shower from Sec. 6.2, the coin operation includes a position check operation. Having extended the position space to two-dimensions, the position check needs to control from both x and y registers corresponding to the number of gluons and quarks, to instruct the ancillary register. The number of gates needed to apply the position check and coin operations for the 2 D quantum walk parton shower is therefore

$$n_{\text{gates}}^{\text{coin}} = N\left(4\left\lceil\log_2\left(N_{\text{max}} + 1\right)\right\rceil + 1\right) \tag{6.3.1}$$

where N_{max} is the maximum number of steps that the algorithm is able to simulate.

The ancillary register like the previous example can be returned to the ground state by reversing the position check operation.

6.3.2 Shift Operation

The shift operation for the QCD quantum walk shower controls now from three different coin registers associated with splittings for: $g \to q\overline{q}$, $g \to gg$ and $q \to qg$, to determine whether each splitting has occurred. Hence after, applying the coin operations to each respective register, tailored incrementing and decrementing operations must be applied controlled from each coin register. The most complicated shift operation is associated with the $g \to q\overline{q}$ splitting channel. It must control from the $|1\rangle$ state of the associated coin register (i.e. a $g \to q\overline{q}$ splitting has taken place) and apply a decrementor to the position space in the x-axis whilst also incrementing in the y-axis in the quark direction. The remaining splittings, following on simply from the shift operation described in Sec. 6.2.2, increment the number of gluons in the x-axis for both the $g \to gg$ and $q \to qg$ splittings of coin register 2, and 3. A schematic outlining these steps is show in Fig. 6.3.

The 2 D framework is useful to visualise as a 2 D lattice through which the quantum walker propagates, readily demonstrated by considering the $q \to qg$ splitting (updating positions on both x and y axes). After N steps of the quantum shower algorithm, the x and y position registers are measured, leading to a determination of the shower particle content after N steps. The movement of the walker in the 2 D lattice is shown visually in Fig. 6.4, where Fig. 6.4a shows the results from a two-step parton shower with the splitting kernels from Eqs. (5.1.1) to (5.1.3). To demonstrate the reach of the walker through the entire lattice, a two-step parton shower where the splitting functions have been enhanced to increase the probability of emission, is shown in Fig. 6.4b.

The number of gates required to implement the $g \to q\overline{q}$ operation at each step is $2\left(\lceil \log_2\left(N_{\max}\right)\rceil\right)^2$, and therefore the number of gates to implement the shift operation

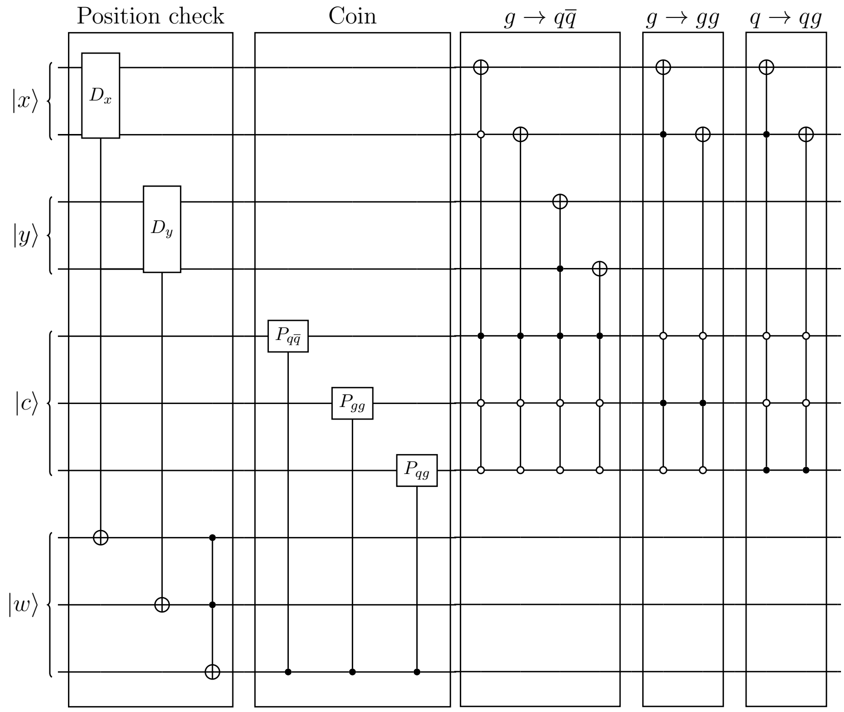

Figure 6.3: Schematic of the quantum circuit for a single step of a discrete QCD, collinear parton shower with the ability to simulate the splittings of gluons and one flavour of quark (taken from Reference [3]). The shower algorithm is split into 3 distinct operations: (1) The position check which determines the position of the walker so that the correct Sudakov form factors are applied in the splitting kernels, (2) the coin operation which applies unitary rotations to a coin register corresponding to the possible splitting kernels, (3) the shift operation updates the position of the walker depending on the particle splitting in the shower step. This step is then repeated iteratively to simulate a full shower process.

for the quantum walk parton shower scales with the number of steps N as

$$n_{\text{gates}}^{\text{shift}} = 4N \left(\lceil \log_2 \left(N_{\text{max}} \right) \rceil \right)^2 . \tag{6.3.2}$$

An important note on the distinction between the quantum parton shower algorithms in chapter 5 and the quantum walker one, is that here there is no preference to be given to the splitting $g \to q\bar{q}$ over $g \to gg$ in the quantum walker case. The Monte Carlo quantum shower also gives preference to the order in which the partons in the shower were produced, according to the position in the register, unlike in the quantum walker case. The quantum walker applies the shift operation, for the case

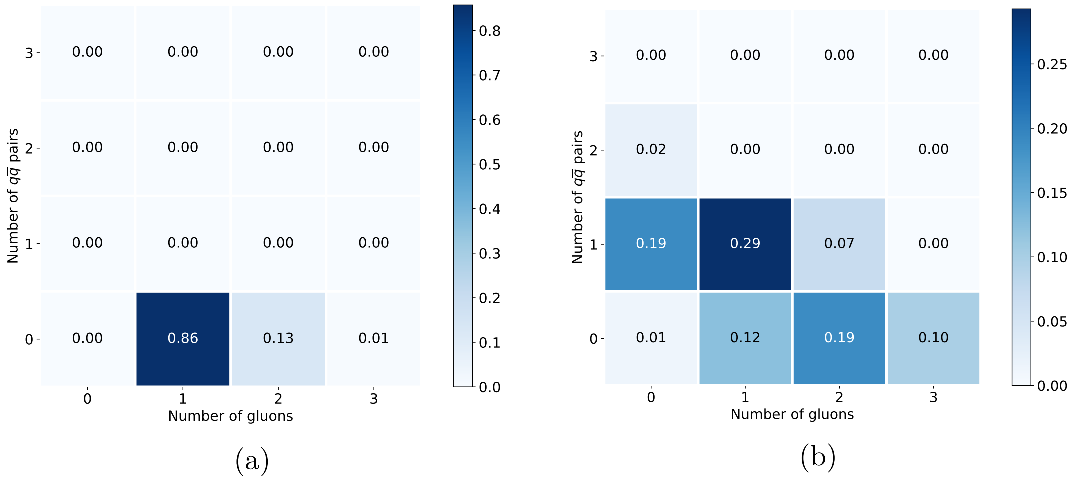

(a) (b)

Figure 6.4: Visualisation of a quantum walk as a parton shower comprising gluons and quarks (Taken from Reference [3]). The quantum walker's position on a 2 D plot corresponds to the number of particles in the parton shower: (a) shows a parton shower using the collinear splitting functions for quarks and gluons, (b) shows a parton shower with modified splitting functions to show how the walker moves in the 2 D lattice.

of multiple splitting channels, only for the case where one coin register is in the $|1\rangle$ state. In the instance of more than one coin register being in the $|1\rangle$ state, the walker remains stationary. Hence, the shift operation is specifically controlled from a single coin register $|1\rangle$ sate (with all other coin registers in the $|0\rangle$ state).

Furthermore, the quantum walker has no knowledge of which specific parton was produced at any given step, highlighting the fact that no preference can be given to any parton for an emission of a parton type. This is a closer reflection of the Monte Carlo approach discussed in Sec. 2.4.2 showing that the quantum walk algorithm as a more natural framework for a parton shower simulation.

6.4 Results

A 31-step quantum walk parton shower has been run on the `ibmq_qasm_simulator` [2] device for 500,000 shots of the algorithm with a gluon as the initial shower particle. The results obtained from the quantum device are shown in Fig. 6.5 and have been compared to a classical simulation using MC event generator of the same set-up.

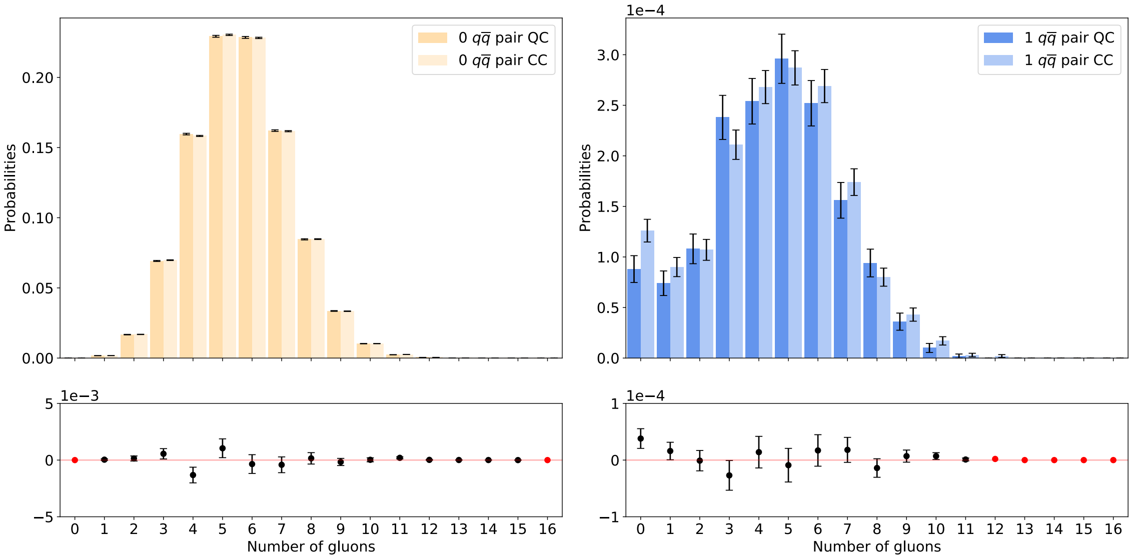

Figure 6.5: Probability distribution of the number of gluons measured at the end of the 31-step parton shower for the classical and quantum algorithms, for the scenario where there are zero quark anti-quark pairs (left) and exactly one quark anti-quark pair (right) in the final state (taken from Reference [3]). The quantum algorithm has been run on the IBMQ 32-qubit quantum simulator [2] for 500,000 shots, and the classical algorithm has been run for 10^6 shots.

Fig. 6.5 shows the number of gluons measured in the final state for two scenarios of fixed $q\bar{q}$ pairs: 0 (on the left) and 1 $q\bar{q}$ pair (on the right). We see that the quantum walk parton shower shows good agreement with the classical algorithm. Since a final state containing one or more quark-antiquark pairs is unlikely, a further modified run is used to validate the algorithm using an enhanced $g \to q\bar{q}$ splitting function to obtain more final states with one or more quark-antiquark pairs. The results from this test are shown in Fig. 6.6 and once again the results show a good agreement with the classical algorithm, confirming that the quantum walk parton shower can replicate a discrete, collinear parton shower successfully. The quantum walker shows a significant increase in the number of steps executed on the quantum device, where the quantum walk parton shower is able to simulate over 15 times the number of shower steps than the quantum Monte Carlo parton shower from chapter 5, thus providing a significant step towards a more realistic quantum simulation of

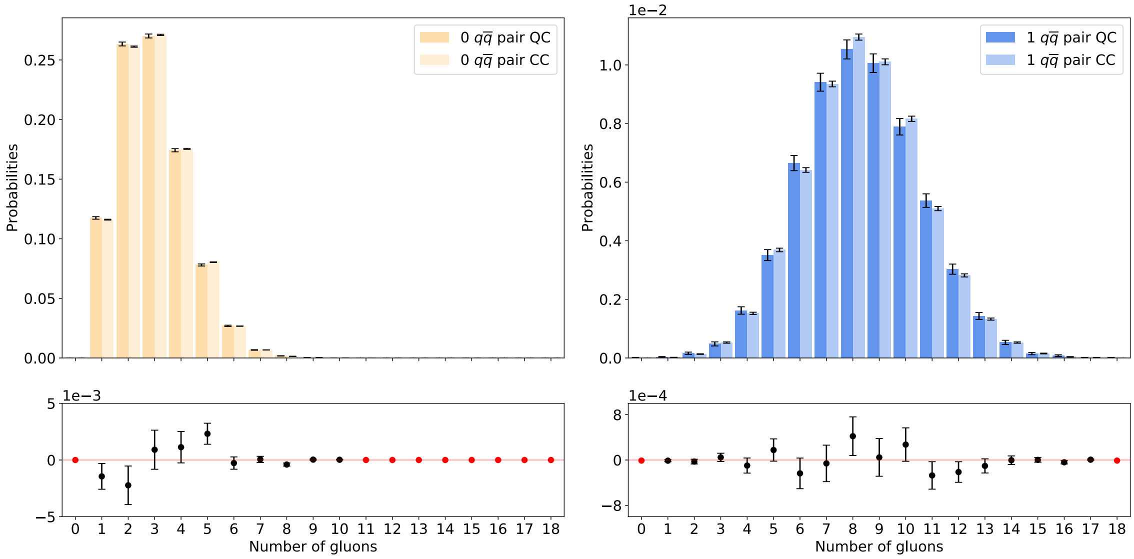

Figure 6.6: Probability distribution of the number of gluons measured at the end of the 31-step parton shower for the classical and quantum algorithms with modified splitting kernels, for the scenario where there are zero quark anti-quark pairs (left) and exactly one quark anti-quark pair (right) in the final state (taken from Reference [3]). The quantum algorithm has been run on the IBMQ 32-qubit quantum simulator [2] for 100,000 shots, and the classical algorithm has been run for 10^6 shots.

parton showers. Furthermore, the quantum walk algorithm scales more efficiently with resources as the number of possible shower steps increases exponentially with the number of qubits and the circuit depth grows linearly with the number of steps, proving the quantum walk to be a natural framework for a quantum implementation of a parton shower.

Chapter 7

Conclusions and Outlook

The simulation of collision events at hadron colliders such as the LHC is incredibly complex, where typically hundreds of particles are produced from the evolution of the collision event towards the final-state long-lived hadrons, leptons, and photons, with these simulations relying heavily on Monte Carlo event generators. The theoretical description of the collisions can be broken down into the initial hard scattering process, and then a subsequent evolution down in energy scale via the parton shower towards the hadronisation scale, $\mathcal{O}\left(\Lambda_{QCD}\right)$, where non-perturbative effects leads to confinement of partons into hadrons. The hard interaction and the parton shower are both perturbative processes and computationally intensive, which together with phase space integration, form a bottleneck in the generation of pseudo-data for ongoing measurements at the LHC. The quantum computing framework provides an alternative computing platform, with the possibility of providing a quantum speedup for these simulations with the use of intrinsic quantum features of the devices. The use of quantum computing is further motivated by the inherent quantum nature of high-energy physics processes, where the quantum computing paradigm provides a natural framework to employ a quantum simulation of these algorithms. In this thesis, we present general and extendable quantum algorithms for two of the key processes of event generation, the hard interaction and the parton shower process. In chapter 4, a quantum algorithm for the computation of helicity amplitudes for the hard process is constructed, and the introduction of helicity registers allows the computation of multiple helicity amplitudes simultaneously. These are calculated for simple 1 → 2, and 2 → 2 processes as proof-of-principle demonstrations with generalisations to n-point tree amplitudes discussed. In chapter 5, an outline of Monte Carlo-inspired quantum parton shower algorithm is given where the quantum algorithm has been used to simulate a simplified 2-step collinear QCD parton shower comprising of one gluon and one quark flavour, which can split according to the collinear DGLAP splitting functions. The quantum Monte Carlo parton shower is shown to have good agreement with the expected rates, however, a discrepancy arises from the $g \to q\bar{q}$ process in the shower history. These channels exhibit an excess in comparison to the analytical rates due to the preference given to the $g \to q\bar{q}$ splitting over the $g \to gg$ splitting in this algorithm's circuit implementation. The quantum Monte Carlo parton shower scales quadratically in both the number of gate operations and qubits, leading to a higher number of CNOT gate counts, providing only a relatively shallow shower depth possible to be simulated on current quantum devices. However, in chapter 6, the quantum parton shower algorithm is reformulated in the quantum walk framework which naturally embeds the algorithm with improved scaling and circuit shower depth. A 31-step collinear toy QCD-parton shower model was implemented on the `ibmq_qasm_simulator`. The quantum walk parton shower also exhibited good agreement with quantum parton shower, simulated using the Monte Carlo approach from Sec. 2.4.2. The quantum walk algorithm was shown to have improved circuit depth and scaling where only 9 qubits and 203 gate operations (144 mutli-qubit and 59 single-qubit gate operations) were required to replicate the two-step shower from chapter 5 in comparison to the 31 qubits and 444 gate operations (275 multi-qubit and 169 single-qubit gate operations) of the original quantum Monte Carlo algorithm, as shown in Reference [3].

Despite the parton shower and helicity algorithms, being far from current realistic shower depths and matrix element calculations on existing event generators, these algorithms are proof-of-principle demonstrations of a quantum parton shower algorithm implementation as well as a novel helicity amplitude calculation providing the first step towards a fully quantum simulation of a LHC collision process. The algorithms are general and extendable, where additional parton flavours can be added trivially to extended registers (in Monte Carlo case) or by increasing the dimension of the walker (for Quantum Walk case). Kinematics can also be considered in future work where kinematic variables will need to be discretised and incorporated within current circuits by extending the Hilbert space of the circuits.

It was found that these algorithms provided unique advantages to the existing helicity amplitude calculations and parton shower process and provides the seeds for future fully developed quantum algorithms which can be used to enhance current classical algorithms of event generators. As mentioned previously, a further opportunity to apply quantum computing to HEP is the simulation of quantum field theories on a quantum computer to explore dynamical properties in the non-perturbative regime of asymptotically free field theories such as QCD. Direct real-time simulation via Hamiltonian formulation of the theories are expected to lead to newfound insights into unexplored regimes of the theories. Constructing resource-efficient algorithms to investigate lower-dimensional quantum field theories on NISQ devices would be an exciting next step, with existing proposals as well demonstrations of proof-of-principle quantum simulations already taking place [101–104].

Appendix A

Quantum logic gates

A.1 Definitions

- **NOT gate**
  - a NOT gate is a single qubit operation which flips the state of the qubit.

$$\mathrm{NOT}|0\rangle = |1\rangle, \qquad \mathrm{NOT}|1\rangle = |0\rangle.$$

The circuit representation of a NOT gate is:

- **CNOT gate**
  - a *controlled*-NOT (CNOT) gate is a two qubit operation which flips the state of a target qubit dependent on the state of a control qubit.

$$\mathrm{CNOT}|00\rangle = |00\rangle, \qquad \mathrm{CNOT}|01\rangle = |01\rangle,$$
$$\mathrm{CNOT}|10\rangle = |11\rangle, \qquad \mathrm{CNOT}|11\rangle = |10\rangle.$$

Here, the first qubit is the control. The circuit representation of a CNOT gate is:

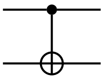

- **Toffoli gate (CCNOT)**
  - A Toffoli gate is a three qubit operation, which is just a further extension of the NOT gate with two control qubits.

$$
\begin{aligned}
\mathrm{CCNOT}|000\rangle &= |000\rangle, & \mathrm{CCNOT}|001\rangle &= |001\rangle,\\
\mathrm{CCNOT}|100\rangle &= |100\rangle, & \mathrm{CCNOT}|010\rangle &= |010\rangle,\\
\mathrm{CCNOT}|110\rangle &= |111\rangle, & \mathrm{CCNOT}|111\rangle &= |110\rangle.
\end{aligned}
$$

The circuit representation of a Toffoli gate is:

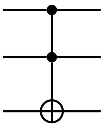

- **Hadamard gate**
  - a Hadamard gate is a purely quantum logic gate and does not have a classical logic gate equivalent. A Hadamard gate is a single qubit operation which puts a qubit into a superposition.

$$\mathrm{H}|0\rangle = \frac{1}{\sqrt{2}}\Big(|0\rangle + |1\rangle\Big), \qquad \mathrm{H}|1\rangle = \frac{1}{\sqrt{2}}\Big(|0\rangle - |1\rangle\Big).$$

The Hadamard gate can be controlled, and so is only applied depending on the state of the control qubit. The circuit representation of a Hadamard gate is:

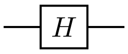

Appendix B

Spinor Helicity Quantum Gate Decompositions

B.1 Dirac and helicity spinor correspondence

The following demonstration of the correspondence between Dirac spinors and Helicity spinors. Fermion and anti-fermion spinors satisfy the Dirac equations such that [92],

$$(\not{p} + m)u(p) = 0, \qquad\qquad (-\not{p} + m)\nu(p) = 0. \tag{B.1.1}$$

where both equations have independent solutions which can be labelled by subscripts $s = \pm$. One can move to a basis where the ± denotes spin up/down along the z-axis, by ensuring that spinors $u_{\pm}$ and $\nu_{\pm}$ are eigenstates of the z-component of the spin-matrix in the rest frame. For massless fermions, ± denotes the helicity, the projection of the spin along the momentum of the particle. These spinors are also associated with the conventional Feynman rules for external fermions, e.g. $\nu_{\pm}(p)$ for an outgoing anti-fermion and $\bar{u}_{\pm}(p)$ for an outgoing fermion.

For the massless case, the Dirac equations reduce to

$$\not{p}\nu_{\pm}(p) = 0 \qquad \bar{u}_{\pm}(p)\not{p} = 0, \tag{B.1.2}$$

where $\nu_{\pm}(p)$ and $u_{\pm}(p)$ are the wavefunctions associated with outgoing anti-fermions and fermions respectively. For this case the wavefunctions are related as $u_{\pm} = \nu_{\mp}$ and $\bar{\nu}_{\pm} = \bar{u}_{\mp}$. The two independent solutions of the Dirac equations can be written as

$$\nu_{+}(p) = \begin{pmatrix} |p]_a \\ 0 \end{pmatrix}, \qquad \nu_{-}(p) = \begin{pmatrix} 0 \\ |p\rangle^{\dot{a}} \end{pmatrix} \tag{B.1.3}$$

and

$$\bar{u}_{-}(p) = \begin{pmatrix} 0 & \langle p|_{\dot{a}} \end{pmatrix}, \qquad \bar{u}_{+}(p) = \begin{pmatrix} [p|^{a} & 0 \end{pmatrix} \tag{B.1.4}$$

where the angle and square spinors are 2-component spinors that satisfy the massless Weyl equation.

The bispinor form of the momenta can be shown by considering [92]

$$\not{p} = \begin{pmatrix} 0 & p_{a\dot{b}} \\ p^{\dot{a}b} & 0 \end{pmatrix} \tag{B.1.5}$$

where

$$p_{a\dot{b}} \equiv p_{\mu}(\sigma^{\mu})_{a\dot{b}} = \begin{pmatrix} -p^0 + p^3 & p^1 - ip^2 \\ p^1 + ip^2 & -p^0 - p^3 \end{pmatrix} \tag{B.1.6}$$

and similarly, $p^{\dot{a}b} \equiv p_{\mu}(\bar{\sigma}^{\mu})^{\dot{a}b}$.

The momentum bispinors $p_{a\dot{b}}$ and $p^{\dot{a}b}$ are 2×2 matrices with determinant

$$\det(p) = -p^{\mu}p_{\mu} = m^2. \tag{B.1.7}$$

and in terms of the Bra-ket helicity spinors they are given by

$$p_{a\dot{b}} = -|p]_a \langle p|_{\dot{b}}, p^{\dot{a}b} = -|p\rangle^{\dot{a}}[p|^b. \tag{B.1.8}$$

B.2 Helicity amplitude gate decompositions

- **$U_{a\rangle}$ gate**
  - The $U_{a\rangle}$ takes the form of a conventional U_3 rotation gate,

$$U_{a\rangle} = U_3(\theta, \phi, \lambda) = \begin{pmatrix} \cos\left(\frac{\theta}{2}\right) & -e^{i\lambda}\sin\left(\frac{\theta}{2}\right) \\ e^{i\phi}\sin\left(\frac{\theta}{2}\right) & e^{i(\phi+\lambda)}\cos\left(\frac{\theta}{2}\right) \end{pmatrix}. \tag{B.2.1}$$

Therefore, the circuit representation is just a qiskit U_3 rotation,

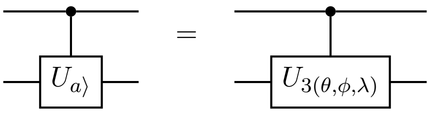

- **$U_{a]}$ gate**
  - The $U_{a]}$ has the matrix form,

$$U_{a]}(\theta, \phi, \lambda) = \begin{pmatrix} -e^{-i\lambda}\sin\left(\frac{\theta}{2}\right) & e^{-i(\phi+\lambda)}\cos\left(\frac{\theta}{2}\right) \\ \cos\left(\frac{\theta}{2}\right) & e^{-i\phi}\sin\left(\frac{\theta}{2}\right) \end{pmatrix} \tag{B.2.2}$$

Therefore, this gate has the circuit representation,

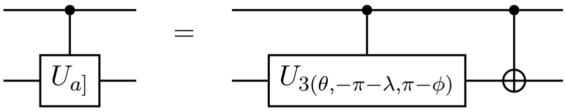

- **$U_{\langle b}$ gate**

- The $U_{\langle b}$ has the matrix form,

$$U_{\langle b}(\theta,\phi) = \begin{pmatrix} -e^{i\phi}\sin\left(\frac{\theta}{2}\right) & \cos\left(\frac{\theta}{2}\right) \\ \cos\left(\frac{\theta}{2}\right) & e^{-i\phi}\sin\left(\frac{\theta}{2}\right) \end{pmatrix} \tag{B.2.3}$$

Therefore, this gate has the circuit representation,

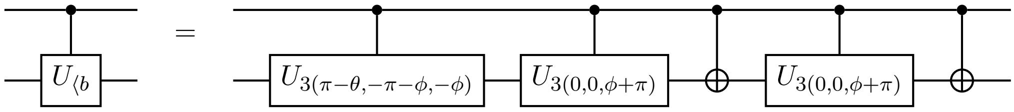

- **$U_{[b}$ gate**
  - The $U_{[b}$ has the matrix form,

$$U_{[b}(\theta,\phi) = \begin{pmatrix} \cos\left(\frac{\theta}{2}\right) & e^{-i\phi}\sin\left(\frac{\theta}{2}\right) \\ -e^{i\phi}\sin\left(\frac{\theta}{2}\right) & \cos\left(\frac{\theta}{2}\right) \end{pmatrix} \tag{B.2.4}$$

Therefore, this gate has the circuit representation,

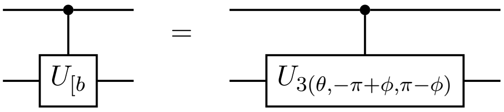

Bibliography

[1] M. A. Nielsen and I. L. Chuang, *Quantum Computation and Quantum Information: 10th Anniversary Edition.* Cambridge University Press, 2010.

[2] IBM Q Team, *IBM Q 32 Simulator v0.1.547*, .

[3] K. Bepari, S. Malik, M. Spannowsky and S. Williams, *Quantum walk approach to simulating parton showers*, *Phys. Rev. D* **106** (2022) 056002, [`2109.13975`].

[4] K. Bepari, S. Malik, M. Spannowsky and S. Williams, *Towards a quantum computing algorithm for helicity amplitudes and parton showers*, *Phys. Rev. D* **103** (2021) 076020, [`2010.00046`].

[5] S. J. Williams, *Event generation on quantum computers*, Ph.D. thesis, Imperial Coll., London, 2023. 10.25560/105867.

[6] ATLAS collaboration, G. Aad et al., *Observation of a new particle in the search for the Standard Model Higgs boson with the ATLAS detector at the LHC*, *Phys. Lett. B* **716** (2012) 1–29, [`1207.7214`].

[7] CMS collaboration, S. Chatrchyan et al., *Observation of a New Boson at a Mass of 125 GeV with the CMS Experiment at the LHC*, *Phys. Lett. B* **716** (2012) 30–61, [`1207.7235`].

[8] S. P. Jordan, K. S. M. Lee and J. Preskill, *Quantum Algorithms for Fermionic Quantum Field Theories.* May, 2014.

[9] L. García-Álvarez, J. Casanova, A. Mezzacapo, I. L. Egusquiza, L. Lamata, G. Romero et al., *Fermion-fermion scattering in quantum field theory with superconducting circuits*, *Phys. Rev. Lett.* **114** (Feb, 2015) 070502.

[10] Z. Davoudi, A. F. Shaw and J. R. Stryker, *General quantum algorithms for Hamiltonian simulation with applications to a non-Abelian lattice gauge theory*, *Quantum* **7** (Dec., 2023) 1213.

[11] A. Kan and Y. Nam, *Lattice Quantum Chromodynamics and Electrodynamics on a Universal Quantum Computer*, `2107.12769`.

[12] A. Ciavarella, N. Klco and M. J. Savage, *Trailhead for quantum simulation of su(3) yang-mills lattice gauge theory in the local multiplet basis*, *Phys. Rev. D* **103** (May, 2021) 094501.

[13] B. Nachman, D. Provasoli, W. A. de Jong and C. W. Bauer, *Quantum algorithm for high energy physics simulations*, *Phys. Rev. Lett.* **126** (Feb, 2021) 062001.

[14] QuNu Collaboration collaboration, T. Li, X. Guo, W. K. Lai, X. Liu, E. Wang, H. Xing et al., *Partonic collinear structure by quantum computing*, *Phys. Rev. D* **105** (Jun, 2022) L111502.

[15] A. Blance and M. Spannowsky, *Quantum Machine Learning for Particle Physics using a Variational Quantum Classifier*, *JHEP* **02** (2021) 212, [`2010.07335`].

[16] A. Blance and M. Spannowsky, *Unsupervised event classification with graphs on classical and photonic quantum computers*, *Journal of High Energy Physics* **2021** (08, 2021) .

[17] K. Terashi, M. Kaneda, T. Kishimoto, M. Saito, R. Sawada and J. Tanaka, *Event classification with quantum machine learning in high-energy physics*, *Computing and Software for Big Science* **5** (12, 2021) .

[18] S. Wu, J. Chan, W. Guan, S. Sun, A. Wang, C. Zhou et al., *Application of quantum machine learning using the quantum variational classifier method to high energy physics analysis at the lhc on ibm quantum computer simulator and hardware with 10 qubits*, *Journal of Physics G: Nuclear and Particle Physics* **48** (07, 2021) .

[19] A. Mott, J. Job, J.-R. Vlimant, D. Lidar and M. Spiropulu, *Solving a higgs optimization problem with quantum annealing for machine learning*, *Nature* **550** (10, 2017) 375–379.

[20] J. Preskill, *Quantum computing in the nisq era and beyond*, *Quantum* (2018) .

[21] P. Langacker, *The standard model and beyond.* 2010.

[22] M. D. Schwartz, *Quantum Field Theory and the Standard Model.* Cambridge University Press, 3, 2014.

[23] M. E. Peskin and D. V. Schroeder, *An Introduction to quantum field theory.* Addison-Wesley, Reading, USA, 1995.

[24] S. Tomonaga, *On a relativistically invariant formulation of the quantum theory of wave fields*, *Prog. Theor. Phys.* **1** (1946) 27–42.

[25] R. P. Feynman, *Space-time approach to non-relativistic quantum mechanics*, *Rev. Mod. Phys.* **20** (Apr, 1948) 367–387.

[26] J. Schwinger, *Quantum electrodynamics. i. a covariant formulation*, *Phys. Rev.* **74** (Nov, 1948) 1439–1461.

[27] C. N. Yang and R. L. Mills, *Conservation of isotopic spin and isotopic gauge invariance*, *Phys. Rev.* **96** (Oct, 1954) 191–195.

[28] W. Pauli, *The connection between spin and statistics*, *Phys. Rev.* **58** (Oct, 1940) 716–722.

[29] J. Schwinger, *The theory of quantized fields. i*, *Phys. Rev.* **82** (Jun, 1951) 914–927.

[30] E. C. Sudarshan, *The fundamental theorem on the connection between spin and statistics., pp 379-86 of Elementary Particle Theory. Svartholm, Nils (ed.). New York, John Wiley and Sons, Inc., 1968.* (10, 1969) .

[31] S. L. Glashow, *Partial-symmetries of weak interactions*, *Nuclear Physics* **22** (1961) 579–588.

[32] S. Weinberg, *A model of leptons*, *Phys. Rev. Lett.* **19** (Nov, 1967) 1264–1266.

[33] S. Weinberg, *Non-abelian gauge theories of the strong interactions*, *Phys. Rev. Lett.* **31** (Aug, 1973) 494–497.

[34] D. J. Gross and F. Wilczek, *Asymptotically free gauge theories. i*, *Phys. Rev. D* **8** (Nov, 1973) 3633–3652.

[35] G. S. Guralnik, C. R. Hagen and T. W. B. Kibble, *Global conservation laws and massless particles*, *Phys. Rev. Lett.* **13** (Nov, 1964) 585–587.

[36] F. Englert and R. Brout, *Broken symmetry and the mass of gauge vector mesons*, *Phys. Rev. Lett.* **13** (Aug, 1964) 321–323.

[37] P. W. Higgs, *Broken symmetries and the masses of gauge bosons*, *Phys. Rev. Lett.* **13** (Oct, 1964) 508–509.

[38] H. Fritzsch, M. Gell-Mann and H. Leutwyler, *Advantages of the Color Octet Gluon Picture*, *Phys. Lett. B* **47** (1973) 365–368.

[39] A. Salam, *Weak and Electromagnetic Interactions*, *Conf. Proc. C* **680519** (1968) 367–377.

[40] S. F. Novaes, *Standard model: An Introduction*, in *10th Jorge Andre Swieca Summer School: Particle and Fields*, pp. 5–102, 1, 1999, `hep-ph/0001283`.

[41] Y. Nambu, *Quasi-particles and gauge invariance in the theory of superconductivity*, *Phys. Rev.* **117** (Feb, 1960) 648–663.

[42] J. Goldstone, *Field theories with "superconductor" solutions*, *Nuovo Cimento* **19** (1961) 154–164.

[43] J. Goldstone, A. Salam and S. Weinberg, *Broken symmetries*, *Phys. Rev.* **127** (Aug, 1962) 965–970.

[44] N. Cabibbo, *Unitary symmetry and leptonic decays*, *Phys. Rev. Lett.* **10** (Jun, 1963) 531–533.

[45] M. Kobayashi and T. Maskawa, *CP Violation in the Renormalizable Theory of Weak Interaction*, *Prog. Theor. Phys.* **49** (1973) 652–657.

[46] A. Buckley, C. White and M. White, *Practical Collider Physics*. 2021, 10.1088/978-0-7503-2444-1.

[47] G. T. Bodwin, *Factorization of the drell-yan cross section in perturbation theory*, *Phys. Rev. D* **31** (May, 1985) 2616–2642.

[48] J. C. Collins, D. E. Soper and G. Sterman, *Factorization for short distance hadron-hadron scattering*, *Nuclear Physics B* **261** (1985) 104–142.

[49] J. C. Collins, D. E. Soper and G. Sterman, *Soft gluons and factorization*, *Nuclear Physics B* **308** (1988) 833–856.

[50] S. Gieseke, D. Grellscheid, K. Hamilton, A. Papaefstathiou, S. Plätzer, P. Richardson et al., *Herwig++ 2.5 release note*, 2011.

[51] C. Bierlich, S. Chakraborty, N. Desai, L. Gellersen, I. Helenius, P. Ilten et al., *A comprehensive guide to the physics and usage of pythia 8.3*, 2022.

[52] Bähr, Manuel, Gieseke, Stefan, Gigg, Martyn A., Grellscheid, David, Hamilton, Keith, Latunde-Dada, Oluseyi et al., *Herwig++ physics and manual*, *Eur. Phys. J. C* **58** (2008) 639–707.

[53] T. Gleisberg, S. Höche, F. Krauss, A. Schälicke, S. Schumann and J.-C. Winter, *Sherpa 1., a proof-of-concept version*, *Journal of High Energy Physics* **2004** (mar, 2004) 056.

[54] S. Marzani, G. Soyez and M. Spannowsky, *Looking Inside Jets: An Introduction to Jet Substructure and Boosted-object Phenomenology.* Springer International Publishing, 2019, 10.1007/978-3-030-15709-8.

[55] R. K. Ellis, W. J. Stirling and B. R. Webber, *QCD and collider physics*, vol. 8. Cambridge University Press, 2, 2011, 10.1017/CBO9780511628788.

[56] S. Hoche and S. Prestel, *The midpoint between dipole and parton showers*, *Eur. Phys. J. C* **75** (2015) 461, [`1506.05057`].

[57] Y. L. Dokshitzer, *Calculation of the Structure Functions for Deep Inelastic Scattering and e+ e- Annihilation by Perturbation Theory in Quantum Chromodynamics.*, *Sov. Phys. JETP* **46** (1977) 641–653.

[58] V. Gribov and L. Lipatov, *Deep inelastic electron scattering in perturbation theory*, *Physics Letters B* **37** (1971) 78–80.

[59] G. Altarelli and G. Parisi, *Asymptotic freedom in parton language*, *Nuclear Physics B* **126** (1977) 298–318.

[60] C. Bierlich, S. Chakraborty, N. Desai, L. Gellersen, I. Helenius, P. Ilten et al., *A comprehensive guide to the physics and usage of pythia 8.3*, *SciPost Physics Codebases* (11, 2022) .

[61] S. Höche, *Introduction to parton-shower event generators*, in *Theoretical Advanced Study Institute in Elementary Particle Physics: Journeys Through the Precision Frontier: Amplitudes for Colliders*, pp. 235–295, 2015, `1411.4085`, DOI.

[62] S. Gieseke, P. Stephens and B. Webber, *New formalism for qcd parton showers*, *Journal of High Energy Physics* **2003** (10, 2003) .

[63] S. Schumann and F. Krauss, *A Parton shower algorithm based on Catani-Seymour dipole factorisation*, *JHEP* **03** (2008) 038, [`0709.1027`].

[64] P. W. Shor, *Polynomial-time algorithms for prime factorization and discrete logarithms on a quantum computer*, *SIAM Journal on Computing* **26** (1997) 1484–1509, [`https://doi.org/10.1137/S0097539795293172`].

[65] L. K. Grover, *A fast quantum mechanical algorithm for database search*, in *Symposium on the Theory of Computing*, 1996, https://api.semanticscholar.org/CorpusID:207198067.

[66] S. P. Jordan, K. S. M. Lee and J. Preskill, *Quantum algorithms for quantum field theories*, *Science* **336** (June, 2012) 1130–1133.

[67] S. P. Jordan, K. S. M. Lee and J. Preskill, *Quantum Algorithms for Fermionic Quantum Field Theories*, `1404.7115`.

[68] J. Preskill, *Simulating quantum field theory with a quantum computer*, *PoS* **LATTICE2018** (2018) 024, [`1811.10085`].

[69] *Ibm quantum-roadmap-2033*, .

[70] A. Einstein, B. Podolsky and N. Rosen, *Can quantum-mechanical description of physical reality be considered complete?*, *Phys. Rev.* **47** (May, 1935) 777–780.

[71] J. S. Bell, *On the einstein podolsky rosen paradox*, *Physics Physique Fizika* **1** (Nov, 1964) 195–200.

[72] A. Aspect, P. Grangier and G. Roger, *Experimental tests of realistic local theories via bell's theorem*, *Phys. Rev. Lett.* **47** (Aug, 1981) 460–463.

[73] A. Aspect, P. Grangier and G. Roger, *Experimental realization of einstein-podolsky-rosen-bohm gedankenexperiment: A new violation of bell's inequalities*, *Phys. Rev. Lett.* **49** (Jul, 1982) 91–94.

[74] A. Aspect, J. Dalibard and G. Roger, *Experimental test of bell's inequalities using time-varying analyzers*, *Phys. Rev. Lett.* **49** (Dec, 1982) 1804–1807.

[75] S. J. Freedman and J. F. Clauser, *Experimental test of local hidden-variable theories*, *Phys. Rev. Lett.* **28** (Apr, 1972) 938–941.

[76] G. Weihs, T. Jennewein, C. Simon, H. Weinfurter and A. Zeilinger, *Violation of bell's inequality under strict einstein locality conditions*, *Phys. Rev. Lett.* **81** (Dec, 1998) 5039–5043.

[77] R. Portugal, *Quantum Walks and Search Algorithms.* Springer Publishing Company, Incorporated, 2013.

[78] E. Farhi and S. Gutmann, *Quantum computation and decision trees*, *Phys. Rev. A* **58** (Aug, 1998) 915–928.

[79] A. Ambainis, E. Bach, A. Nayak, A. Vishwanath and J. Watrous, *One-dimensional quantum walks*, in *Proceedings of the Thirty-Third Annual ACM Symposium on Theory of Computing*, STOC '01, (New York, NY, USA), p. 37–49, Association for Computing Machinery, 2001, DOI.

[80] J. Kempe, *Quantum random walks: An introductory overview*, *Contemporary Physics* **44** (2003) 307–327, [`https://doi.org/10.1080/00107151031000110776`].

[81] Y. Aharonov, L. Davidovich and N. Zagury, *Quantum random walks*, *Phys. Rev. A* **48** (Aug, 1993) 1687–1690.

[82] A. M. Childs, R. Cleve, E. Deotto, E. Farhi, S. Gutmann and D. A. Spielman, *Exponential algorithmic speedup by a quantum walk*, in *Proceedings of the Thirty-Fifth Annual ACM Symposium on Theory of Computing*, STOC '03, (New York, NY, USA), p. 59–68, Association for Computing Machinery, 2003, DOI.

[83] T. G. Wong, *Faster search by lackadaisical quantum walk*, *Quantum Information Processing* **17** (mar, 2018) 1–9.

[84] A. Nayak and A. Vishwanath, *Quantum walk on the line*, 2000.

[85] D. Meyer, *From quantum cellular automata to quantum lattice gases*, *Journal of Statistical Physics* **85** (02, 1999) .

[86] M. Szegedy, *Quantum speed-up of markov chain based algorithms*, in *45th Annual IEEE Symposium on Foundations of Computer Science*, pp. 32–41, 2004, DOI.

[87] N. Shenvi, J. Kempe and K. B. Whaley, *Quantum random-walk search algorithm*, *Phys. Rev. A* **67** (May, 2003) 052307.

[88] P. Wocjan and A. Abeyesinghe, *Speedup via quantum sampling*, *Phys. Rev. A* **78** (Oct, 2008) 042336.

[89] R. D. Somma, S. Boixo, H. Barnum and E. Knill, *Quantum simulations of classical annealing processes*, *Phys. Rev. Lett.* **101** (Sep, 2008) 130504.

[90] M. Troyer and U.-J. Wiese, *Computational complexity and fundamental limitations to fermionic quantum monte carlo simulations*, *Phys. Rev. Lett.* **94** (May, 2005) 170201.

[91] C. Gattringer and K. Langfeld, *Approaches to the sign problem in lattice field theory*, *International Journal of Modern Physics A* **31** (03, 2016) .

[92] H. Elvang and Y.-t. Huang, *Scattering Amplitudes in Gauge Theory and Gravity.* Cambridge University Press, 2015.

[93] IBM Q Team, *IBM Q Santiago 5 Qubit Quantum Computer v1.0.3*, .

[94] D. Maitre and P. Mastrolia, *S@M, a Mathematica Implementation of the Spinor-Helicity Formalism*, *Comput. Phys. Commun.* **179** (2008) 501–574, [`0710.5559`].

[95] F. Cachazo, P. Svrcek and E. Witten, *MHV vertices and tree amplitudes in gauge theory*, *JHEP* **09** (2004) 006, [`hep-th/0403047`].

[96] R. Britto, F. Cachazo, B. Feng and E. Witten, *Direct proof of tree-level recursion relation in Yang-Mills theory*, *Phys. Rev. Lett.* **94** (2005) 181602, [`hep-th/0501052`].

[97] S. J. Parke and T. R. Taylor, *Amplitude for n-gluon scattering*, *Phys. Rev. Lett.* **56** (Jun, 1986) 2459–2460.

[98] P. P. Rohde, G. K. Brennen and A. Gilchrist, *Quantum walks with memory provided by recycled coins and a memory of the coin-flip history*, *Phys. Rev. A* **87** (May, 2013) 052302.

[99] V. Giovannetti, S. Lloyd and L. Maccone, *Quantum random access memory*, *Phys. Rev. Lett.* **100** (Apr, 2008) 160501.

[100] B. L. Douglas and J. B. Wang, *Efficient quantum circuit implementation of quantum walks*, *Phys. Rev. A* **79** (May, 2009) 052335.

[101] L. Funcke, T. Hartung, K. Jansen and S. Kühn, *Review on Quantum Computing for Lattice Field Theory*, *PoS* **LATTICE2022** (2023) 228, [`2302.00467`].

[102] J. F. Haase, L. Dellantonio, A. Celi, D. Paulson, A. Kan, K. Jansen et al., *A resource efficient approach for quantum and classical simulations of gauge theories in particle physics*, *Quantum* **5** (Feb., 2021) 393.

[103] D. Paulson, L. Dellantonio, J. F. Haase, A. Celi, A. Kan, A. Jena et al., *Simulating 2d effects in lattice gauge theories on a quantum computer*, *PRX Quantum* **2** (Aug, 2021) 030334.

[104] T. Felser, P. Silvi, M. Collura and S. Montangero, *Two-dimensional quantum-link lattice quantum electrodynamics at finite density*, *Phys. Rev. X* **10** (Nov, 2020) 041040.